Valley-selective circular dichroism from substrate induced symmetry breaking in two-dimensional silver

Bachelorarbeit

im Fach Physik

zur Erlangung des akademischen Grades
Bachelor of Science

Institut für Theoretische Physik und Astrophysik
Mathematisch-Naturwissenschaftliche Fakultät
Christian-Albrechts-Universität zu Kiel

vorgelegt von

Melina Seidel
Matrikelnummer: 1147825

im November 2022

First examiner:	Prof. Dr. Fabio Caruso
Second examiner:	Prof. Dr. Eckhard Pehlke

Abstract

A silver monolayer can be synthesized with an intercalation between silicon carbide and epitaxial buffer bilayer graphene. The goal of this thesis is to establish whether the interaction with the substrate can alter the fundamental symmetry (e.g. inversion symmetry) of the system, and to which extend new properties can arise. We find that silicon carbide breaks the inversion symmetry of two-dimensional silver. This can be directly observed by the Rashba effect. Furthermore, we show that the substrate induces valley-selective circular dichroism in two-dimensional silver. This property is very interesting for the field of valleytronics.

Zusammenfassung

Zwei-dimensionales Silber kann zwischen Siliziumkarbid und zwei expitaxial gewachsenen Lagen von Graphen synthetisiert werden. Das Ziel dieser Arbeit ist es festzustellen, ob die Wechselwirkung mit dem Substrat die fundamentale Symmetrie (zum Beispiel die Inversionssymmetrie) des Systems verändern kann, und in welchem Umfang neue Eigenschaften entstehen können. Es zeigt sich, dass Siliziumkarbid die Inversionssymmetrie von zwei-dimensionalem Silber bricht, was direkt am Rashba-Effekt beobachtet werden kann. Darüber hinaus zeigen wir, dass das Substrat Valley-selektiven zirkularen Dichroismus hervorruft. Diese Eigenschaft ist sehr interessant für das Forschungsgebiet der Valleytronik.

Contents

1 Introduction

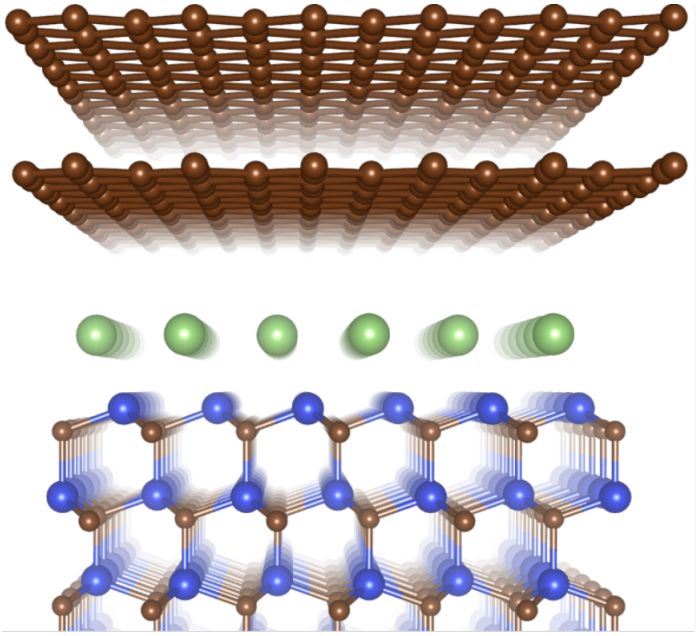

Figure 1.1: Atomic structure of intercalated silver between bilayer graphene and silicon carbide [18].

Two-dimensional materials are very interesting because their properties can be fundamentally different from the bulk counterparts. This work investigates two-dimensional silver, which is a promising material for plasmon-based technologies such as biosensors and waveguides [6]. The investigations presented in this thesis are motivated by the recent synthesis of two-dimensional silver, in the heterostructures illustrated in Fig. 1.1, by the group of J. Robinson at Penn State University[18]. A monolayer of silver atoms can be intercalated between silicon carbide (SiC) and bilayer graphene.
Interestingly, the synthesized silver monolayer is semiconducting due to its hybridization with the underlying SiC. The intercalation process further generates a quasi-free-standing graphene bilayer, which functions as a capping layer and prevents oxidation of the confined epitaxial metals. Nonetheless, it does not significantly influences the electronic properties [18].
Two-dimensional silver films are synthesized using the process illustrated in Fig. 1.2. First, the epitaxial graphene layer is created when silicon atoms sublime from

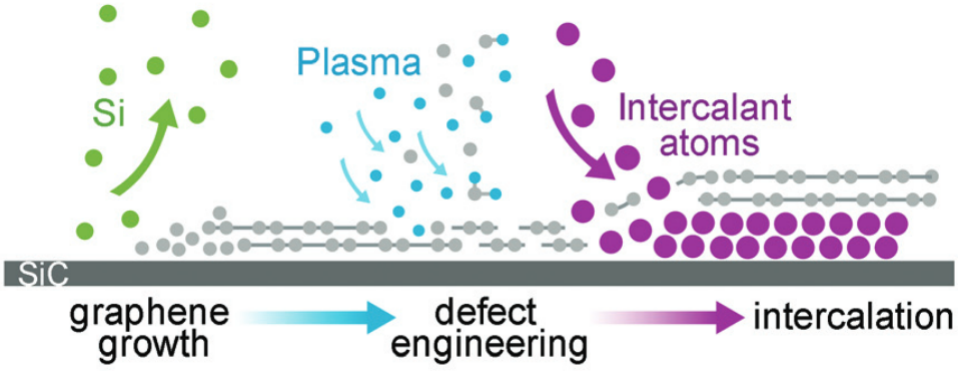

Figure 1.2: Schematic intercalation process for synthesizing material between SiC and bilayer graphene [6].

the surface of SiC, leaving behind carbon atoms which reconstruct epitaxially with the SiC surface. This process enables the realization of large-area graphene layers, but also result in the formation of a carbon buffer layer that is partially covalent bound to the SiC surface [6].

Following the synthesis in Fig. 1.2, defects in the expitaxial graphene layers are generated by exposing epitaxial graphene to an O_2/He plasma treatment. The substrate SiC with the graphene layers is then placed face down over metallic silver powder and heated up. The intercalation of silver atoms physically and electronically separates the carbon layer from SiC, resulting in the formation of quasi-free standing epitaxial graphene layers [6].

Cross-sectional scanning transmission electron microscopy (STEM) of intercalated silver samples shows one layer of silver atoms located between graphene and the SiC substrate (Fig. 1.3). This layer is confirmed to consist of silver atoms through energy dispersive X-ray spectroscopy mapping (EDS) [6].

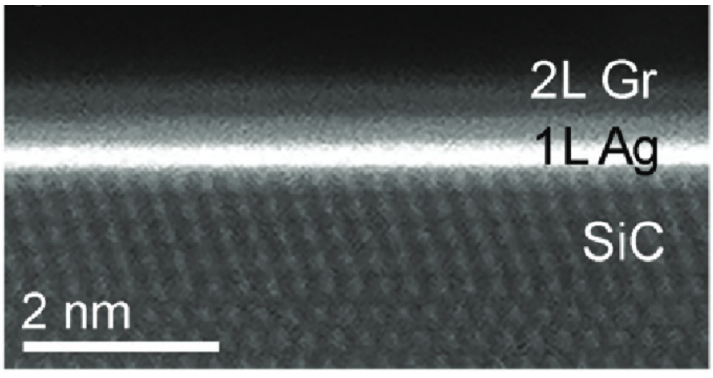

Figure 1.3: Cross-sectional STEM showing one layer of silver atoms between epitaxial graphene and SiC [6].

The commonly observed sharp $6\sqrt{3} \times 6\sqrt{3}R30^\circ$ patterns for bilayer graphene on SiC become a fuzzy ring, suggesting a decoupling of the bilayer graphene and SiC due to the silver intercalation. Scanning tunneling microscope studies, however, still exhibit a quasi 6×6 superstructure superimposed on the graphene 1×1 lattice (Fig. 1.4). That is consistent to the assumption that the silver monolayer has the same lattice constant as SiC [18].

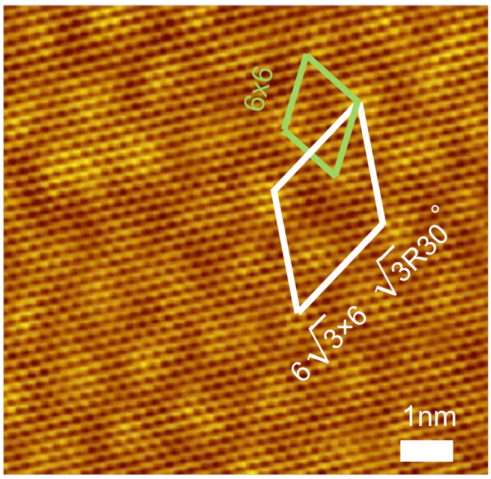

Figure 1.4: STM topography [18].

Silicon carbide is an interesting material for high-temperature, radiation-resistant, power and high-speed electronics. The reason is that it has a wide band gap of 2.01 eV, a high critical avalanche breakdown field, a high electron drift saturation rate, high thermal stability, chemical inertness and excellent mechanical properties [23]. This work is interested in valley-selective circular dichroism. Silver in its structure as a monolayer grown from epitaxial graphene is centrosymmetric, namely it has an inversion symmetry. With the interaction with a substrate, in this case SiC, the symmetry can be broken. In this thesis, I explore the influence of substrate-induced symmetry breaking on the electronic properties of two-dimensional silver. The results in this thesis show that this leads to a different absorption of circular polarized light in different regions of the Brillouin zone, which is called *valley-selective circular dichroism*. This property is interesting for *Valleytronics*. There, one influences the probability of optical transitions at extreme points in the band structure [2]. The main result of this work is that the substrate SiC breaks the inversion symmetry and induces the emergence of valley physics in two-dimensional silver.
In chapter 2, I introduce the theoretical and practical methods of density functional theory employed throughout this work. The results are split up in chapter 3 and 4. One deals with the electronic properties, mainly the band structures, and the other one with valley-selective circular dichroism and symmetry breaking.

2 Density functional theory

This chapter is an introduction to density functional theory. Staring with the main theoretical concepts we will move on to the procedure of a practical DFT calculation, discuss important aspects for calculations with surfaces and have a look at computational details. The chapter is based on [11], [22] and [10].

2.1 Units

In this work, Hartree atomic units are used. They are defined as

$$\begin{aligned} 1 \text{ Ha} &= 27.2114 \text{ eV} = 4.3597 \cdot 10^{-18} \text{ J}, && (2.1)\\ 1 \text{ bohr} &= 0.529177 \text{ Å} = 0.529177 \cdot 10^{-10} \text{ m}, && (2.2)\\ 1 \text{ a.u.ofmass} &= 9.10938291 \cdot 10^{-31} \text{ kg}, && (2.3)\\ & && (2.4) \end{aligned}$$

where 'Ha' stands for Hartree and 'a.u.' for atomic unit. The advantage of this units are that the following fundamental physical constants are expressed as the numeric value one:

- Reduced Planck constant $\hbar$
- The absolute value of the elementary charge $|e|$
- Electron mass m_e.

2.2 The Schrödinger equation

The information of a physical system is all contained in the Hamiltonian which is the central quantity for any theoretical treatment. For microscopic particles like electrons, the adequate description is given by the laws of quantum mechanics. Therefore, the Schrödinger equation has to be solved.
In general, materials consist of electrons and nuclei. Therefore, the fundamental interaction is the electrostatic interaction. Furthermore, this work is mostly interested in valence electrons, so relativistic effects can be neglected. The corresponding Hamiltonian for the nonrelativistic Schrödinger equation is

$$\hat{H} = \hat{T}_{nucl} + \hat{T}_{el} + \hat{V}_{nucl-nucl} + \hat{V}_{nucl-el} + \hat{V}_{el-el}. \quad (2.5)$$

$\hat{T}_{nucl}$ and $\hat{T}_{el}$ are the operators for the kinetic energy of the nuclei and the electrons, respectively. The other operators describe the electrostatic interaction between the nuclei and the electrons. Neglecting spins, the terms are:

$$\hat{T}_{nucl} = \sum_I -\frac{\nabla_I^2}{2M_I} \tag{2.6}$$

$$\hat{T}_{el} = \sum_i -\frac{\nabla_i^2}{2} \tag{2.7}$$

$$\hat{V}_{nucl-nucl} = \frac{1}{2}\sum_{I\neq J} \frac{Z_I Z_J}{|\mathbf{R}_I - \mathbf{R}_J|} \tag{2.8}$$

$$\hat{V}_{nucl-el} = \sum_{i,I} -\frac{Z_I}{|\mathbf{r}_i - \mathbf{R}_I|} \tag{2.9}$$

$$\hat{V}_{el-el} = \frac{1}{2}\sum_{i\neq j} \frac{1}{|\mathbf{r}_i - \mathbf{r}_j|} \tag{2.10}$$

$$\tag{2.11}$$

Atoms are numbered by capital letter indices and Z_I stands for the charge of the I-th nuclei. The factor of $\frac{1}{2}$ in $\hat{V}_{nucl-nucl}$ and $\hat{V}_{el-el}$ prevents that the interaction of two nuclei or electrons are counted twice.
It is only possible to solve the many-body Schrödinger equation

$$\hat{H}\Phi = E\Phi \tag{2.12}$$

for a system consisting of few electrons or atoms. For solids, approximations are required.

2.3 Born-Oppenheimer approximation

The mass of a proton or a neutron is more than 1800 times the mass of an electron. As a consequence, the electrons are more than 40 times faster than a proton for the same kinetic energy. The differences increase for heavier nuclei. This leads to the central idea of the *Born-Oppenheimer* or *adiabatic approximation* to separate the time scale of processes involving electrons and nuclei.
The electronic Hamiltonian $\hat{H}_{el}$ for fixed nuclear coordinates $\{\mathbf{R}\}$ is

$$\hat{H}_{el}(\{\mathbf{R}\}) = \hat{T}_{el} + V_{nucl-nucl} + \hat{V}_{nucl-el} + \hat{V}_{el-el}, \tag{2.13}$$

where $\{\mathbf{R}\}$ is a parameter defining the electronic Hamiltonian. Moreover, $V_{nucl-nucl}(\{\mathbf{R}\})$ is not an operator but a number.
The Schrödinger equation for the electrons is then

$$\hat{H}_{el}(\{\mathbf{R}\})\psi(\mathbf{r},\{\mathbf{R}\}) = E_{el}(\{\mathbf{R}\})\psi(\mathbf{r},\{\mathbf{R}\}). \tag{2.14}$$

The eigenenergy $E_{el}(\{\mathbf{R}\})$ is called the *Born-Oppenheimer energy surface* and taken to be the potential for nuclear motion. The movement of the nuclei is described by the atomic Schrödinger equation

$$\{\hat{T}_{nucl} + E_{el}(\mathbf{R})\}\tilde{\psi}(\mathbf{R}) = E_{nucl}\tilde{\psi}(\mathbf{R}), \tag{2.15}$$

where $\tilde{\psi}$ denotes the nuclear wave function. Neglecting quantum effects, the classical equation of motions are solved for the atomic motion:

$$M_I \frac{\partial^2}{\partial t^2}\mathbf{R}_I = -\frac{\partial}{\partial \mathbf{R}_I}E_{el}(\mathbf{R}). \tag{2.16}$$

The force acting on the atoms is given by the *Hellmann-Feynman theorem*

$$\mathbf{F}_I = -\frac{\delta}{\delta \mathbf{R}_I}E_{el}(\mathbf{R}) = \langle\psi(\mathbf{r},\{\mathbf{R}\})|\frac{\delta}{\delta \mathbf{R}_I}\hat{H}_{el}(\{\mathbf{R}\})|\psi(\mathbf{r},\{\mathbf{R}\})\rangle. \tag{2.17}$$

The Born-Oppenheimer approximation is more accurate for a small parameter $\frac{m}{M}$ and very successful in the theoretical description of processes at surfaces. For insulator and semiconductors, a finite amount of energy is needed to excite electronic states. It can be shown that electronically nonadiabatic transitions are rather improbable. For metals, small excitation energies can occur but the strong coupling of the electronic states in the conduction band leads to short lifetimes so that their influence is often limited.

2.4 Density functional theory

To solve the Schrödinger equation for electrons (2.14), further approximations are needed.
As a first approximation, the electron wave function for fixed positions of the nuclei can be expressed as a product of individual electron wave functions

$$\psi(\mathbf{r},\{\mathbf{R}\}) = \psi_1(\mathbf{r})\cdot\psi_2(\mathbf{r})...\cdot\psi_N(\mathbf{r}), \tag{2.18}$$

which is called the *Hartree product*. The density of electrons at a particular position in space is given by

$$n(\mathbf{r}) = 2\sum_i \psi_i^*(\mathbf{r})\psi_i(\mathbf{r}). \tag{2.19}$$

$\psi_i^*(\mathbf{r})\psi_i(\mathbf{r})$ is the probability that an electron in the individual wave function ψ_i is located at position $\mathbf{r}$. The summation runs over all the individual electron wave functions that are occupied by electrons. The factor of two is motivated by the Pauli exclusion principle because each individual electron wave function can be occupied by two electrons with different spin.
There are two fundamental mathematical theorems for the field of density functional theory proved by Kohn and Hohenberg. The first theorem is:

> "The ground-state energy from Schrödinger's equation is a unique functional of the electron density."[22]

A functional is a function from a vector space into the scalar field. The ground-state energy E can be expressed as $E[n(\mathbf{r})]$.
This observation is remarkable because, while the energy of any quantum state is generally a functional of the entire wave function, $\psi(\mathbf{r}_1, \mathbf{r}_2, ..., \mathbf{r}_N)$, which contains 3N variables, the ground-state energy depends only on $n(\mathbf{r})$, which is a function of three variables only.
The first theorem proves that a functional of the electron density exists that can be used to solve the Schrödinger equation.
An important property of the functional is defined by the second Hohenberg-Kohn theorem:

> "The electron density that minimizes the energy of the overall functional is the true electron density corresponding to the full solution of the Schrödinger equation."[22]

That means that one can find the ground state energy approximately by systematically varying the electron density.
Furthermore, it is proved that there exists a universal functional of the density, $F[n(\mathbf{r})]$, which is independent of an external potential $V(\mathbf{r})$, such that the expression

$$E[n] \equiv \int V(\mathbf{r})n(\mathbf{r})d^3\mathbf{r} + F[n(\mathbf{r})] \tag{2.20}$$

has a minimum which is the correct ground-state energy associated with $V(\mathbf{r})$ [13]. The functional can be written in terms of the single-electron wave function $\psi_i(\mathbf{r})$ because these functions collectively define the electron density $n(\mathbf{r})$. Moreover, it can be split up in collections of known terms, $E_{known}[\{\psi_i\}]$, and everything else, $E_{XC}[\{\psi_i\}]$:

$$E[\{\psi_i\}] = E_{known}[\{\psi_i\}] + E_{XC}[\{\psi_i\}] \tag{2.21}$$

where

$$\begin{aligned} E_{known}[\{\psi_i\}] = -\sum_i \int \psi_i^* \frac{\Delta^2}{2}\psi_i d^3\mathbf{r} + \int V(\mathbf{r})n(\mathbf{r})d^3\mathbf{r} \\ +\frac{1}{2}\int\int \frac{n(\mathbf{r})n(\mathbf{r\prime})}{|\mathbf{r}-\mathbf{r\prime}|}d^3\mathbf{r}d^3\mathbf{r\prime} + E_{ion} \end{aligned} \tag{2.22}$$

The known terms are, in order, the electron kinetic energy, the Coulomb interaction between the electrons and the nuclei, the Coulomb interaction between the electrons, and the Coulomb interactions between nuclei.
$E_{XC}[\{\psi_i\}]$ is called the *exchange-correlation functional* and it is defined to include all the quantum mechanical effects that are not included in the terms of $E_{known}[\{\psi_i\}]$.

Kohn and Sham showed that the right electron density can be found by solving a set of equations in which each equation only involves a single electron.
The Kohn-Sham equations have the form

$$\left[-\frac{1}{2}\Delta^2 + V(\mathbf{r}) + V_H(\mathbf{r}) + V_{XC}(\mathbf{r})\right]\psi_i(\mathbf{r}) = \epsilon_i\psi_i(\mathbf{r}). \tag{2.23}$$

The solutions of the Kohn-Sham equations are single-electron wave functions that depend on only three spatial variables. The potential V defines the interaction between an electron and the collection of atomic nuclei. V_H is called the *Hartree potential* and is defined by

$$V_H(\mathbf{r}) = \int \frac{n(\mathbf{r\prime})}{|\mathbf{r} - \mathbf{r\prime}|} d^3\mathbf{r\prime}. \tag{2.24}$$

It describes the Coulomb repulsion between the electron and the total electron density given by all electrons in the system. Since the electron also contributes to the total electron density, there is an unphysical self-interaction between the electron and itself. The correction for this and several effects is given by the *exchange and correlation potential*, V_{XC}. It can formally be defined as a "functional derivative" of the exchange-correlation energy:

$$V_{XC}(\mathbf{r}) = \frac{\partial E_{XC}(\mathbf{r})}{\partial n(\mathbf{r})}. \tag{2.25}$$

For solving the Kohn-Sham equations, the exchange-correlation functional $E_{XC}[n]$ must be specified. The true form of the functional is not known, except for the situation of the uniform electron gas, where the electron density is constant at all points in space. The *local density approximation* (LDA) is an approximation of the exchange-correlation potential in the way that it is the exchange-correlation potential from the uniform electron gas at the electron density observed at that point:

$$V_{XC}(\mathbf{r}) = V_{XC}^{\text{electron gas}}[n(\mathbf{r})]. \tag{2.26}$$

Another approach is called *generalized-gradient approximation* (GGA) and it uses information about the local electron density and the local gradient in the electron density. Nevertheless, this approach is not always more accurate than LDA. There are many ways in which information from the gradient of the electron density can be included in a GGA functional. Thus, there is a large number of different GGA functionals. For this work, the *Perdew-Burke-Ernzerhof functional* (PBE) is used. There are other functionals that include even more physical information. It depends on the physical system which functional fits the best.
The solution of the Kohn-Sham equations requires an iterative procedure, because the Hartree potential and an exchange-correlation potential depend on the electron density. The density, in turn, is calculated from the wave functions resulting from the Kohn-Sham equations. Therefore, the problem is usually treated in an iterative way as outlined in the following algorithm which is also illustrated on the next page:

- First, calculate the potential of the nuclei.
- Second, define an initial, trial electron density $n(\mathbf{r})$.
- With this density, calculate the Hartee potential V_H and the exchange-correlation potential V_{XC}.
- Sum up all these potentials to a total potential V_{tot} and solve the Kohn-Sham equations.
- With the resulting Kohn-Sham single-particle wave functions, calculate the electron density.
- Compare the calculated electron density with that one used for the Hartree potential. If they are the same up to a certain degree of accuracy, it can be used to compute the total energy. If the two densities are different, then the trial electron density must be updated in some way.

This method is *self-consistent*.

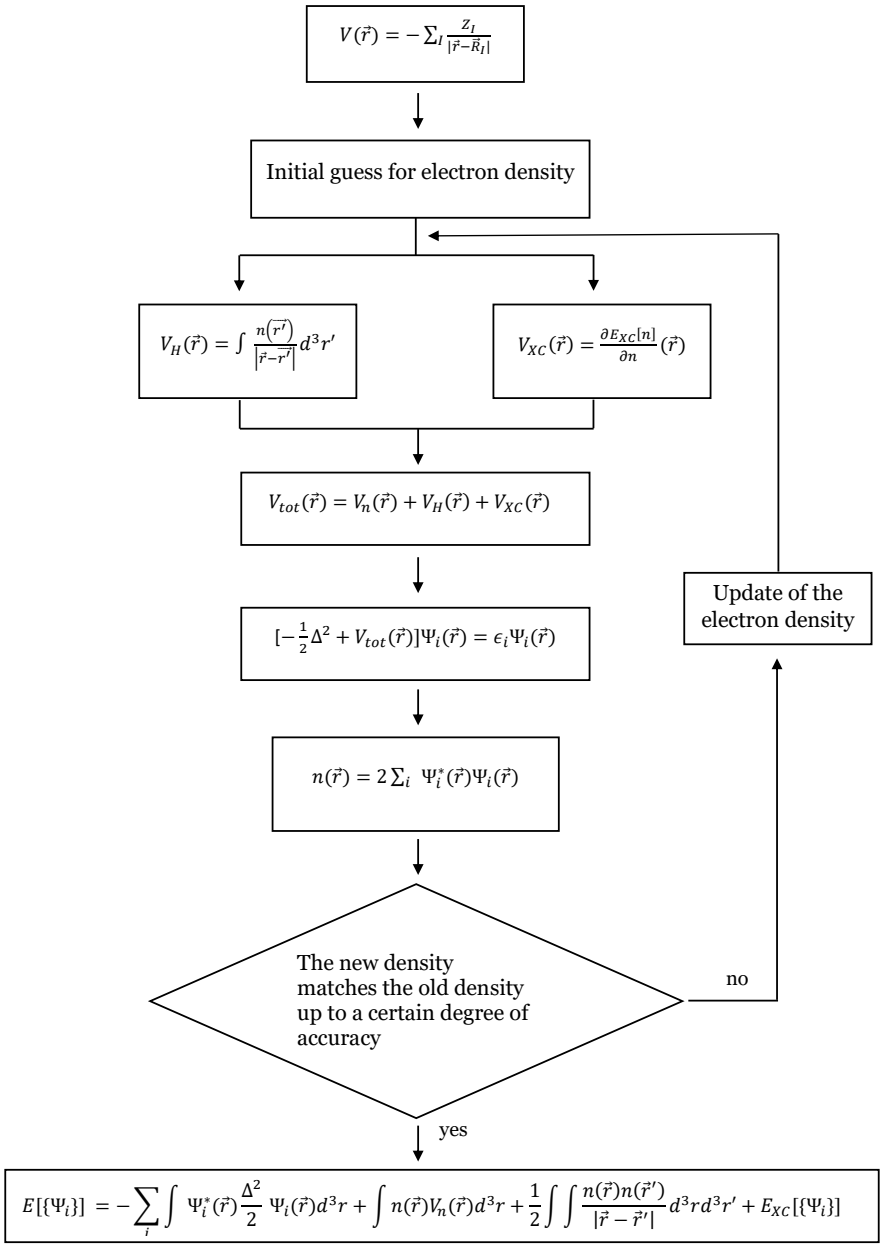

Figure 2.1: Algorithm for calculating the ground-state energy of a system according to the density functional theory.

2.5 DFT calculations for surfaces of solids

In practice, a computer code is used for DFT calculations. In the following we describe the numerical procedure employed to investigate the physical properties of a surface. The positions of all atoms in a crystal must be defined.

An ideal solid with a surface is infinite in two dimensions, but finite along the surface normal. In order to define a corresponding atomistic model, it may seem natural to take advantage of periodic boundary conditions in two dimensions, but not the third. There are codes, in which this technique is implemented, but it is more common to study a surface using a code that applies periodic boundary conditions in all three dimensions, and this approach will be discussed. Therefore, one has to design a supercell which includes empty space above the atoms. This model is called *slab model* since, when the supercell is repeated in all three dimensions, it defines a series of stacked slabs of solid material separated by vacuum space. The supercell defines two surfaces. It is important that there is enough vacuum space to make sure that the interaction between the top of one slab and the bottom of the next slab is negligible. For each slab there are several layers of atoms and the more layers are used the higher is the physical accuracy of the result but it costs more computational time so a compromise has to be found.

In Fig. 2.2, there is an example illustrated for the slab model. Theoretically, the structure is infinite in the direction of the plane but for visualization only a finite number of supercell repetitions can be shown. In this case it is a surface of silicon carbide, which plays an important role for this work. The thickness of one slab is equal to the length of the supercell of SiC. This is because the unit cell of this 6H-polytype of SiC contains already 20 layers of atoms which is sufficient to model a SiC surface. The vacuum used for the slab model in this work has a length of 25 Å. Convergency tests of the total energy showed that this is enough to approximate that there are no interactions between the slabs, see Fig. 6.1 in the appendix.

While the construction of a bulk is expected to be stable, the surface might not be in its optimal physical configuration. Because of the asymmetry of bulk on the one side and vacuum on the other side, the distance between the atoms in the surface layer and the layer underneath might be smaller compared to the bulk. This phenomenon is called *surface relaxation* and implies that the relaxed surface has a lower energy than the original, ideal surface. One can find the geometry of the relaxed surface by performing an energy minimization as a function of the positions of the atoms in the supercell. Therefore, the positions of the atoms at the bottom of the supercell are kept constant because these atoms represent the bulk.

Futhermore, surface atoms can also form new bonds which is called *surface reconstruction*. The reconstructed surface defines the global minimum in the energy of the surface, but the bulk termination of the surface can lead to a different local minimum in energy.

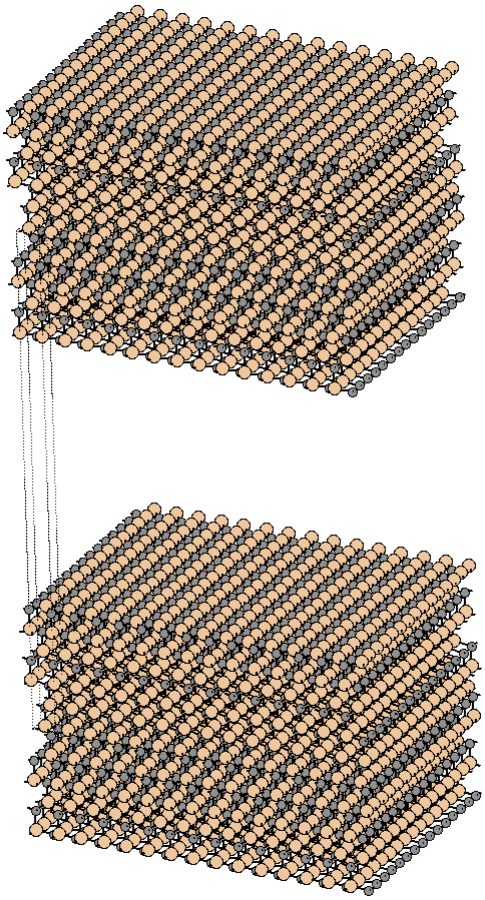

Figure 2.2: Illustration of the slab model applied to silicon carbide.

2.6 Convergency

For a DFT calculation, a series of numerical approximations is needed, for example integrals in multidimensional space must be evaluated by examining the function to be integrated at a finite collections of points and solutions that formally are expressed as infinite sums must be truncated to finite sums. In each numerical approximation of this kind the result come closer to the exact solution by using more computational resources. This convergency is important for DFT calculations. The results are only trustworthy if the calculation does converge. One has to find a compromise between the accuracy of the results and the time needed for the calculation. To make an estimation of the difference to the exact solution, one has to make calculations and start with low and move to high accuracy. Now, one can decide to take a accuracy which has a certain error to the one with the high accuracy. But one need to keep in mind that the exact solution of the DFT calculation is not identical to the exact solution of the Schrödinger equation because the precise form of the exchange-correlation functional is unknown.

2.7 Reciprocal space and k points

In this work, DFT calculations are applied to arrangements of atoms that are periodic in space. The lattice vectors of the unit cell are in general $\mathbf{a}_1, \mathbf{a}_2$ and $\mathbf{a}_3$. The *Bloch's theorem* must be fulfilled for the solution of this periodic system, namely that the solution can be expressed as a sum of terms with the form

$$\Phi_{\mathbf{k}}(\mathbf{r}) = e^{i\mathbf{k}\cdot\mathbf{r}} u_{\mathbf{k}}(\mathbf{r}), \tag{2.27}$$

where $u_{\mathbf{k}}(\mathbf{r})$ is periodic in space with the same periodicity as the unit cell

$$u_{\mathbf{k}}(\mathbf{r} + n_1\mathbf{a}_1 + n_2\mathbf{a}_2 + n_3\mathbf{a}_3) = u_{\mathbf{k}}(\mathbf{r}) \quad \text{for } n_1, n_2, n_3 \in \mathbb{Z}. \tag{2.28}$$

It is possible to solve the Schrödinger equation for each value of $\mathbf{k}$ independently. The functions $e^{i\mathbf{k}\cdot\mathbf{r}}$ are called plane waves. The space of vectors $\mathbf{r}$ is called real space, and the space of vectors $\mathbf{k}$ is called reciprocal space or k space. The reciprocal lattice vectors $\mathbf{b}_1, \mathbf{b}_2$ and $\mathbf{b}_3$ are defined so that $\mathbf{a}_i \cdot \mathbf{b}_j$ is 2π if $i = j$ and 0 otherwise:

$$\mathbf{b}_i = 2\pi \frac{\mathbf{a}_j \times \mathbf{a}_k}{\mathbf{a}_i \cdot (\mathbf{a}_j \times \mathbf{a}_k)}. \tag{2.29}$$

The primitive cell in reciprocal space is called the *Brillouin zone* (BZ). It contains several high-symmetry points with special significance. The most important of these is the Γ point where $\mathbf{k} = 0$. The volume of the BZ, V_{BZ}, and the volume of the primitive cell in real space defined by the Wigner-Seitz construction, V_{cell}, are related by

$$V_{BZ} = \frac{(2\pi)^3}{V_{cell}}. \tag{2.30}$$

For DFT calculations, there is less effort in evaluating integrals of the form

$$\overline{g} = \frac{V_{cell}}{(2\pi)^3} \int_{BZ} g(\mathbf{k}) d\mathbf{k}. \tag{2.31}$$

This integral is defined in reciprocal space and it integrates only over the possible values of $\mathbf{k}$ in the BZ. To evaluate this numerically, a method is used which separates the integral in smaller intervals and makes approximations for them.
The following points also apply to multidimensional integrals. It is a quotation from [22].

1. "Integrals can be approximated by evaluating the function to be integrated at a set of discrete points and summing the function values with appropriate weighting for each point."

2. "Well-behaved numerical methods of this type will give more accurate results as the number of discrete points used in the sum is made larger. In the limit of using a very large number of points, these numerical methods converge to the exact results for the integral."

3. "Different choices for the placement and weighting of the functional evaluations can give dramatic differences in the rate the numerical methods converge to the exact integral."

2.7.1 Choosing k points in the Brillouin zone

Integrals such as (2.31) cost a lot of computational effort in DFT calculations. In most DFT packages, one can choose k points based on the method developed by Monkhorst and Pack in 1976 [19]. It only needs a specification how many k points are to be used in each direction in reciprocal space.

Using the symmetry, integrals can be evaluated in a reduced portion of the BZ that can then be extended without approximation to fill the entire BZ. This reduced region in reciprocal space is called the *irreducible Brillouin zone* (IBZ) and it can greatly reduce the numerical effort required to perform integrals in k space. Nonetheless, the convergency of the calculations in k space is related to the density of k points in the full BZ. Convergency tests are needed to find a adequate number of k points to use. In general for bulk calculations, the choice of k points should define a set of k points with equal density in each direction in reciprocal space. For surfaces, it is usual for slab calculations with long vacuum regions in the supercell to use an $\mathrm{M} \times \mathrm{N} \times 1$ k point mesh, where M and N are chosen to adequately sample k space in the plane of the surface ($\mathrm{M}, \mathrm{N} \in \mathbb{N}$). The k point density of the calculation in this work is approximately $280/\text{Å}^{-3}$.

In a metal, the BZ can be divided into regions that are occupied and unoccupied by electrons. The surface in k space that separates these two regions is called *Fermi surface*. This is a significant complication for calculating integrals in k space because the functions that are integrated change discontinuously from nonzero values to zero at the Fermi surface. If no special efforts are made in calculating these integrals, very large numbers of k points are needed to get well-converged results.

One method is called the *tetrahedron method*. The idea is to use the discrete set of k points to define a set of tetrahedron that fill reciprocal space and to define the function being integrated at every point in a tetrahedron using interpolation. The function to be integrated has a simple form at all points in k space and the integral can then be evaluated using the entire space, not just discrete points.

Another approach to the discontinuous integrals that appear for metals are *smearing methods*. The idea is to force the function being integrated to be continuous by "smearing" out the discontinuity. An example of a smearing function is the Fermi-Dirac function. Ideally, a method should be used that extrapolates the final result to the limit where the smearing is eliminated.

2.7.2 Energy cutoffs

As mentioned above, the Bloch's theorem states that the solutions of the Schrödinger equation have the form

$$\Phi_{\mathbf{k}}(\mathbf{r}) = \exp(i\mathbf{k} \cdot \mathbf{r}) u_{\mathbf{k}}(\mathbf{r})$$

where $u_{\mathbf{k}}(\mathbf{r})$ is periodic in space with the same periodicity as the unit cell. The periodicity of $u_{\mathbf{k}}(\mathbf{r})$ means that it can be expanded in terms of a spacial set of plane

waves

$$u_{\mathbf{k}}(\mathbf{r}) = \sum_{\mathbf{G}} c_{\mathbf{G}} \exp[i\mathbf{G} \cdot \mathbf{r}], \tag{2.32}$$

where the summation is over all vectors defined by $\mathbf{G} = m_1\mathbf{b}_1 + m_2\mathbf{b}_2 + m_3\mathbf{b}_3$ with $m_1, m_2, m_3 \in \mathbb{Z}$. Combining the two equations above gives

$$\Phi_{\mathbf{k}}(\vec{r}) = \sum_{\mathbf{G}} c_{\mathbf{k}+\mathbf{G}} \exp[i(\mathbf{k} + \mathbf{G})\mathbf{r}]. \tag{2.33}$$

Evaluating the solution at even a single point in k space involves a summation over an infinite number of possible values of $\mathbf{G}$. According to the Schrödinger equation, $\Phi_{\mathbf{k}}(\vec{r})$ are solutions with the kinetic energy

$$E_{kin} = \frac{1}{2}|\mathbf{k} + \mathbf{G}|^2. \tag{2.34}$$

The solutions with higher energies are associated with the core electrons. Since we are mostly interested in valence electrons, it is usual to truncate the infinite sum above to include only solutions with kinetic energies less than some value:

$$E_{cut} = \frac{1}{2}G_{cut}^2. \tag{2.35}$$

The infinite sum then reduces to

$$\Phi_{\mathbf{k}}(\vec{r}) = \sum_{|\mathbf{G}+\mathbf{k}|<G_{cut}} c_{\mathbf{k}+\mathbf{G}} \exp[i(\mathbf{k} + \mathbf{G})\mathbf{r}]. \tag{2.36}$$

This expression includes slightly different numbers of terms for different values of $\mathbf{k}$. The *cutoff energy* E_{cut} that must be defined whenever a DFT calculation is performed. Therefore, convergency tests are necessary to find an adequate value.

2.7.3 Pseudopotentials

Large energy cutoffs must be used to include plane waves that have short wave lengths in real space and hence are associated with core electrons. However, core electrons do not play an important role for chemical properties but they are dominated by the less tightly bound valence electrons. Therefore, the properties of the core electrons can be approximated in a way that could reduce the number of plane waves necessary in a calculation.
A so called *pseudopotential* replaces the electron density from a chosen set of core electrons with a smoothed density. It is chosen to match various important physical and mathematical properties of the true ion core. There are libraries of pseudopotentials that include an entry for most elements in the periodic table. For every pseudopotential there is a minimum cutoff energy that should be used in calculations. If this cutoff energy is high, the pseudopotential is called hard. Otherwise, if

the cutoff energy is low, the pseudopotential is more computationally efficient and is called soft.
One class of pseudopotentials are *ultrasoft pseudopotentials* (USPPs) based on work by Vanderbilt [26]. These peudopotentials require substantially lower cutoff energies than alternative approaches. Another class are *projector augmented-wave* (PAW) which were originally introduced by Blöchl and later adapted for plane-wave calculations by Kresse and Joubert. Kresse and Joubert compared USPP, PAW and all-electron calculations for small molecules and extended solids [16]. Their work shows that well-constructed USPPs and the PAW method give results that are in good agreement with all-electron calculations. In materials with strong magnetic moments or with atoms that have large differences in electro negativity, the PAW approach gives more reliable results than USPPs.
Norm-conserving pseudopotentials (NCPPs) are supported by many ab-initio codes. Their formalism is relatively simple and robust. As compared to the more recently developed USPP and the PAW, on the one hand calculations using NCPPs usually require a larger kinetic energy cutoff making them less efficient. On the other hand, little is known about the reliability of these two approaches when applied beyond standard ground state calculations. In contrast NCPPs have been used for decades in different ab-initio fields [25].
The *PseudoDojo* is an open source project for developing and systematically testing pseudopotentials. The pseudopotential files are available on the PseudoDojo web-interface [1]. Van Setten et al. (2018) have constructed a new NCPP table, using the PBE exchange–correlation functional, distributed within the PseudoDojo (PD-PBE), using the new framework of the *optimized norm-conserving Vanderbilt pseudopotential* (ONCVPSP). The main advantage of ONCVPSP is that it produces NCPPs that are usually softer and they are more accurate than traditional NCPPs [25].
The pseudopotential used for this work is generated using ONCVPSP code by D.R. Hamann [25].

2.8 QUANTUM ESPRESSO

For this work, all calculations are done with QUANTUM ESPRESSO. It is a modular and open-source software project for quantum simulations of materials and is described in [9]. ESPRESSO is an acronym for *opEnSource Package for Reasearch in Electronic Structure, Simulation and Optimization.* It is freely available under the terms of the GNU General Public License[2]. The project is coordinated by the QUANTUM ESPRESSO foundation, which was formed by many research centers and groups all over the world. For supercomputers today, parallelization is a key concept, and with QUANTUM ESPRESSO it is achieved using both MPI and OpenMP parallelization.

[1] `pseudo-dojo.org`
[2] `http://www.gnu.org/licenses/`

QUANTUM ESPRESSO is collection of computer codes for first-priciple electronic calculations based on DFT, plane waves and pseudopotentials. The codes are constructed around the use of periodic boundary conditions but finite systems are also treated using supercells. QUANTUM ESPRESSO can be used for any crystal structure or supercell and for metal as well as for insulators. There are different pseudopotentials and exchange-correlation functionals available [9].
At the beginning of a calculation with QUANTUM ESPRESSO, an input file has to be created where the geometry of the material, all parameters and the type of calculation are defined. There are several of parameters to specify the calculation. Important parameters are the cutoff energy parameter and the number of k points in every direction. For both parameters a convergency test is needed. Other parameters can include spin orbit coupling, a special symmetry of the material or a smearing to allow the occupation of states over the Fermi energy. One has to decide for a pseudopotential and an exchange-correlation functional. For self-consistent calculations, QUANTUM ESPRESSO follows the algorithm introduced in the beginning of this chapter. For relaxation calculations, the forces between the atoms are needed and calculated with the Hellmann-Feynman-Theorem (2.17).

3 Electronic properties of two-dimensional silver on silicon carbide

In this chapter, the band structure for silicon carbide with a silver monolayer is calculated. The graphene bilayers are quasi free-standing and are neglected for the calculations because they do not influence the electronic properties significantly. At the beginning, we will have a closer look on the different components of the material.

3.1 Silver monolayer

As a bulk, silver has a fcc crystal structure. Nonetheless, silver is constructed as a hexagonal monolayer for this work. The reason is that the silver atoms are bounded on SiC. As a further consequence, the lattice constant of the monolayer is equal to the lattice constant of SiC [18].
The structure of the silver monolayer is schematically shown in Fig. 3.1.

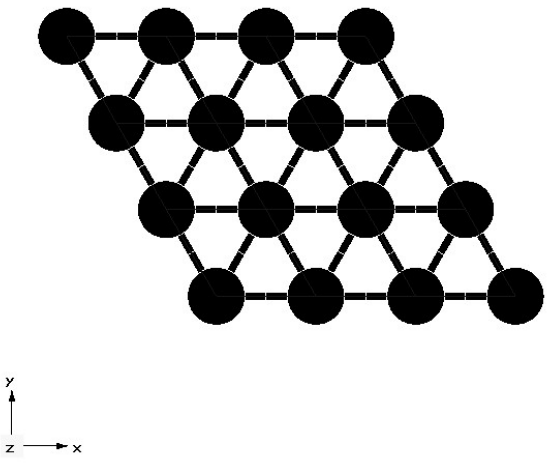

Figure 3.1: Hexagonal structure of the silver monolayer.

The crystallographic point group in the Schoenflies notation is D_{6h} and 6/mmm in the Hermann-Mauguin notation, so it is hexagonal and has a six-fold rotational axis

plus six twofold axes perpendicular to that axis. In addition, there is a mirror plane perpendicular to the six-fold axis [1].
The band structure is calculated for the $\Gamma - \mathrm{M} - \mathrm{K} - \Gamma$ - path in the first BZ and is shown in Fig. 3.2. Convergency tests have been done to determine the cutoff energy as $E_{\mathrm{cutoff}} = 70$ Ry ≈ 952 eV and the number of k points in the x- and y-direction as 15. As for a monolayer, the number of k points in the z-direction is one. The code uses the symmetry of the structure to reduce the number of k points, in this case to 27 k points in total. Furthermore, spin-orbit coupling is considered in this calculation. The energy error threshold is 4×10^{-9} eV/atom.

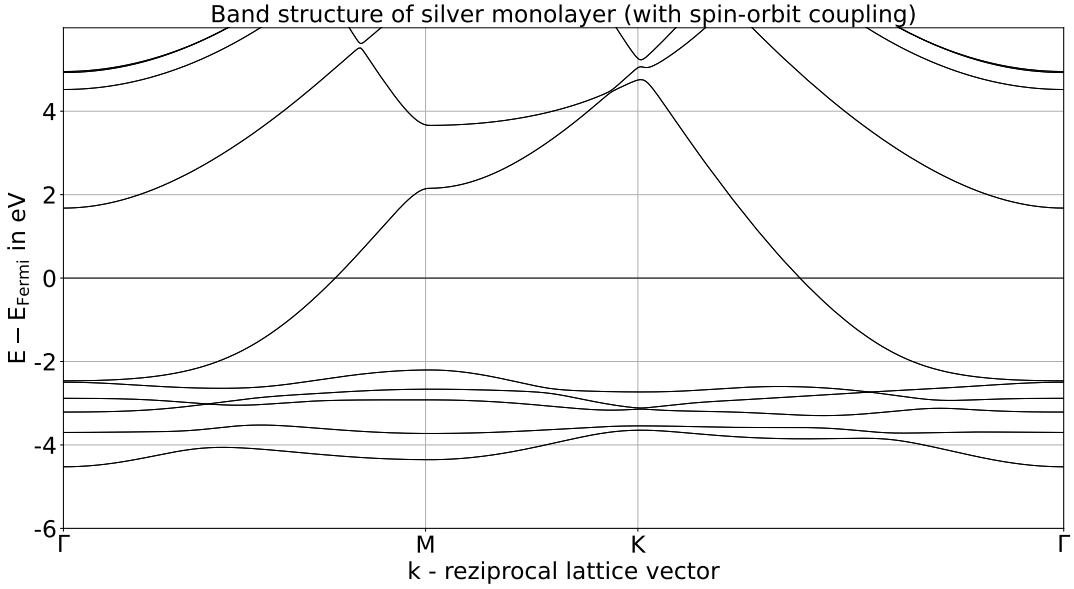

Figure 3.2: Band structure of silver monolayer with spin-orbit coupling

Because there is no band gap, two-dimensional silver is a metal. One band crosses the Fermi energy and shows a maximum at the high symmetry point K and a saddle point at M.

3.2 Silicon carbide

Silicon carbide exists in many polytype modifications, which are derivatives of hexagonal and rhombohedral closed-package crystal lattices. All of them follow the laws of close ball packing and are binary structures built of identical layers [23].
The unit cell of SiC is taken from the website "The Materials Project" [15]. For this work, the 6H-SiC polytype is chosen because it provides the most stable conditions. The unit cell is shown in Fig. 3.3 a).

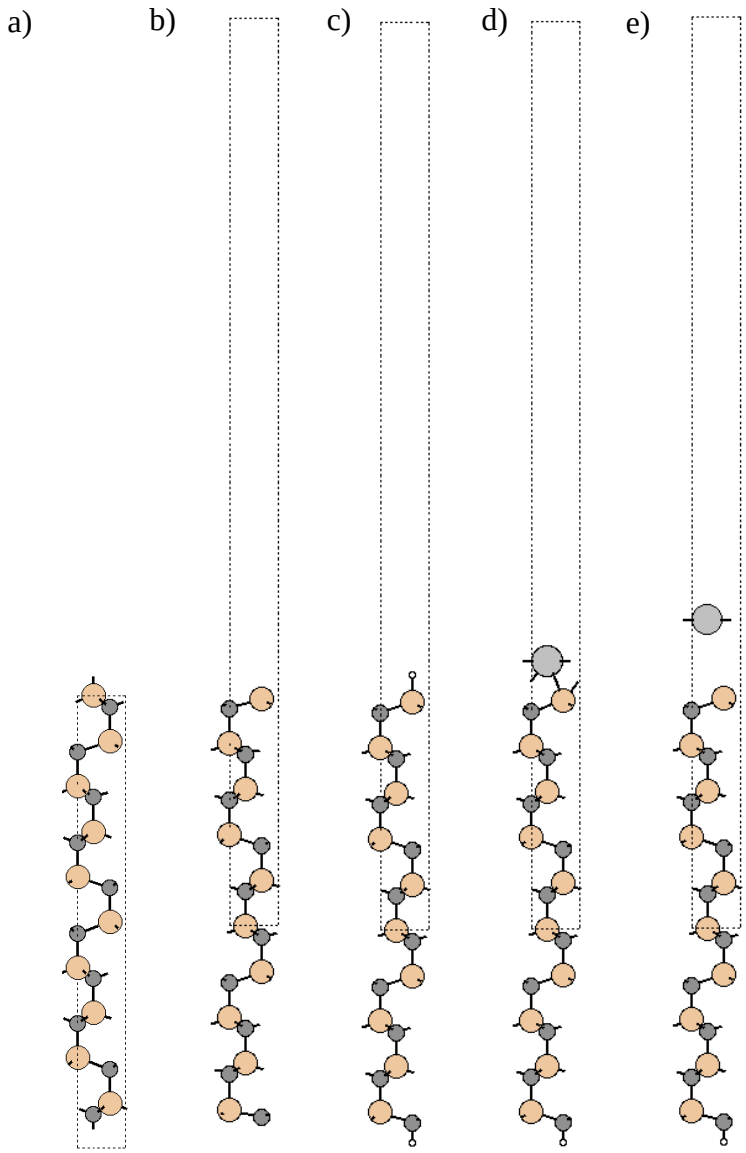

Figure 3.3: The supercells are shown where silicon has beige colour, carbon is dark grey, silver is light grey and hydrogen is white: a) supercell for the SiC bulk b) for the SiC surface c) for the SiC surface with H termination d) for the SiC surface with silver monolayer and H termination. In the z coordinate, the silver atoms have a distance of 2.153 Å to the silicon atoms. e) The distance of the silver atoms is increased to 4.337Å.

The crystal system is trigonal and the lattice system hexagonal. The unit cell contains 20 atoms. The lattice constants are [1]

- $a_1 = 3.09$ Å
- $a_2 = 3.09$ Å
- $a_3 = 25.31$ Å

This material, as a bulk, has no inversion center and belongs to the crystallic point group C_{3v} in Schoenflies notation and 3m in the Hermann-Mauguin notation. The group has an three-fold rotation axis and three mirror planes parallel to the axis of rotation [1].
The band structure is calculated with $E_{\text{cutoff}} = 70$ Ry ≈ 952 eV and $12 \times 12 \times 2$ k points (Fig. 3.4). In real space, the unit cell is longer in the z direction than in the x and y direction. In reciprocal space, it is the opposite and this is the reason that there are less k points in the z direction. Spin-orbit coupling is included. One can see a band gap of approximately 2 eV.

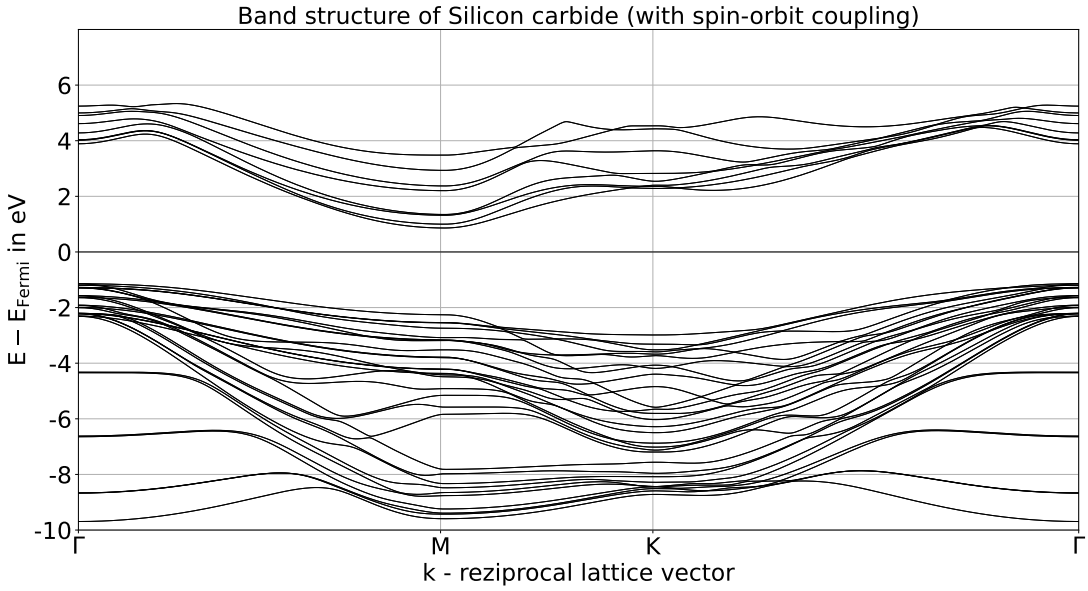

Figure 3.4: Band structure of silicon carbide with spin-orbit coupling.

The occupation is determined by the Fermi energy. The chemical potential $\mu(T)$ is located within the band gap because the number of electrons must be equal to the number of wholes. The Fermi-energy is defined as $E_{\text{Fermi}} = \lim_{T \to 0} \mu(T)$.

[1] `https://materialsproject.org/materials/mp-568656?chemsys=Si-C`

3.3 Silicon carbide slab

To create a surface, the unit cell of SiC has to be truncated. We choose an atomistic model which reproduces the crystal structure of Fig. 1.1, the structure is shown in Fig. 3.3 b). Furthermore, a vacuum of about 25 Å is added above the surface to avoid interactions among the periodic replicas of the SiC slabs. For one slab, one unit cell is taken because the unit cell already contains enough atoms to approximate a bulk. The more atoms are in the supercell the more expensive the calculation becomes. Before the calculation of the band structure, the structure was relaxed. Fig. 3.3 shows already the relaxed structure. Mainly the surface atoms get slightly closer to the bulk (about 0.2 Å). The band structure is shown in Fig. 3.5 with $E_{\text{cutoff}} = 70$ Ry ≈ 952 eV and $12 \times 12 \times 1$ k points. Here, only one k point is used in z-direction because it is a surface and the real space distance in z-direction of the slabs is larger.

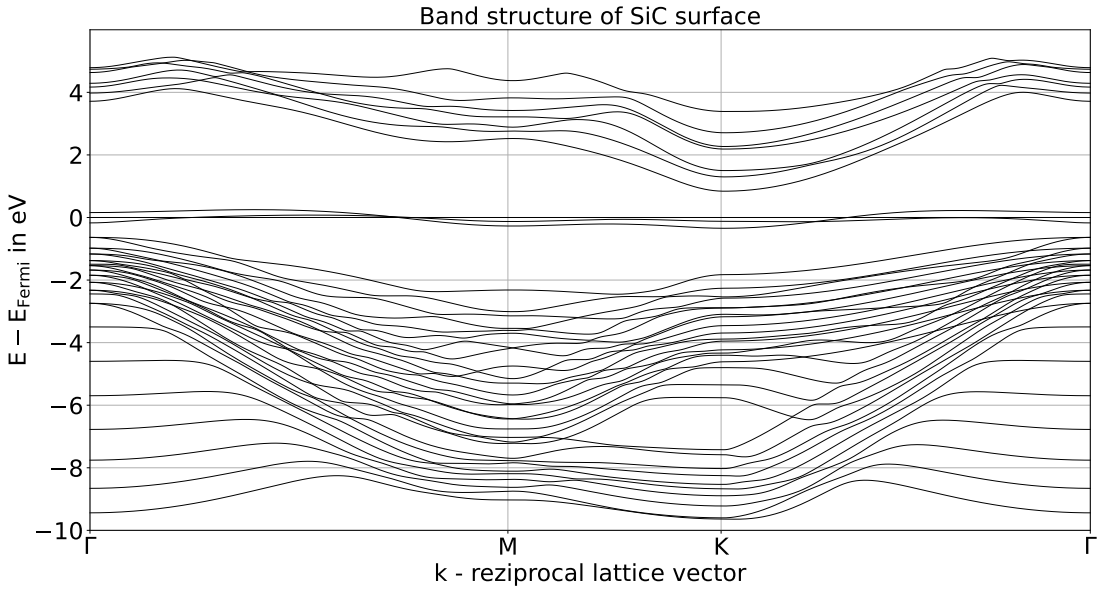

Figure 3.5: Band structure of Silicon carbide slab.

In comparison with the bulk band structure, the structures look very similar but there are two flat bands near the Fermi energy. These bands are the result of dangling bonds at the two surfaces. At the bottom surface the carbon atom lacks a bonding and at the top surface it is the silicon atom. To compensate this effect, a hydrogen atom is added at each surface.
The structure, shown in Fig. 3.3 c), is relaxed, but this time the lowest carbon atom was fixed in its position because it should represent the bulk and not a surface. The band structure is calculated for the $\Gamma - \mathrm{K} - \mathrm{M} - \overline{\mathrm{K}} - \Gamma$ path (Fig. 3.6) which becomes important for the evaluation of valley-selective circular dichroism.

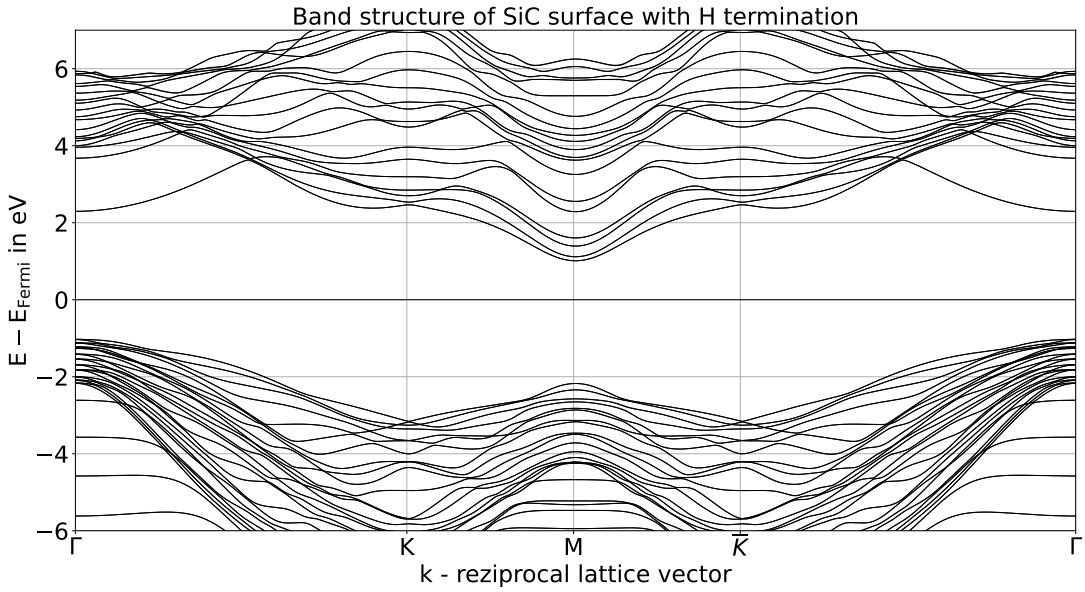

Figure 3.6: Band structure of Silicon carbide surface with H termination.

3.4 Silicon carbide with two-dimensional silver

On top of the SiC surface comes a single layer of silver atoms. The silver atoms have the same lattice constants as SiC to avoid stresses. Lee et al.[18] found that the energetically most favorable position for the silver atoms is directly above the second topmost layer of C atoms. The next most stable configuration is higher in energy by 8 eV per atom. Both configurations are realistic but this work only considers the most stable position. The structure with the locations of the silver atoms is shown from above in Fig. 3.7. The silicon atoms have beige colour, the carbon atoms are dark grey and the silver atoms are light grey. The silver atoms are at the top of the structure. The silicon atoms without a carbon atom above have a distance of 2.153 Å and the carbon atoms have a distance of 2.807 Å in the z direction to the silver atom. The silicon atoms under the carbon atoms have a distance of 4.707 Å.

Relaxation calculations showed that only the z-coordinate of the silver atom changes to create an energetically optimal configuration whereas the x- and y-coordinates stay equal to the second topmost layer of C atoms. This supports that the position, found by Lee et al.[18], is stable. The relaxed structure is shown in Fig. 3.3 d). Again, a hydrogen atom is added at the bottom surface to prevent dangling bonds and the lowest carbon atoms was fixed in its position during the relaxation calculation.

Like SiC, this material has also no inversion center and belongs to the crystallographic point group C_{3v} in Schoenflies notation and 3m in the Hermann-Mauguin notation which means that it has an three-fold rotation axis and three mirror planes

parallel to the axis of rotation [1].

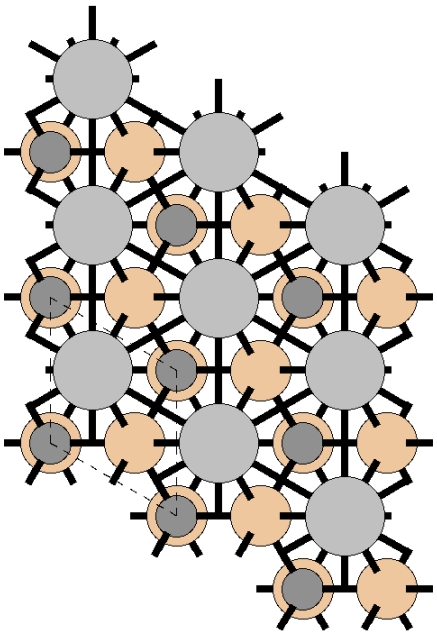

Figure 3.7: Structure of SiC with silver monolayer seen from above. The silicon atoms have beige colour, the carbon atoms are dark grey and the silver atoms are light grey. 3×3 supercells are shown.

For this material, convergency tests for the cutoff energy and the k points are added in the appendix (Fig. 6.3 and 6.2). We choose the same parameters as for the SiC slab with $E_{\text{cutoff}} = 70$ Ry ≈ 952 eV and $12 \times 12 \times 1$ k points and the band structure is shown in Fig. 3.8. It shows that this material is a semiconductor with a small band gap of about 0.24 eV. This is due to the hybridization of the silver monolayer with the underlying SiC [18]. Again, there is a characteristic band with a saddle point at M and a maximum at K like for two-dimensional silver (Fig. 3.2). Thus, this band can be attributed to silver.
Experimental data for the band structure of a silver monolayer intercalated between silicon carbide and epitaxial buffer layer graphene is reported by Rosenzweig et al.[20]. They used angle-resolved photoelectron spectroscopy. Fig. 3.9 shows the band structure of Fig. 3.8 in green superimposed to the experimental results.
The band structure in the $\Gamma - \mathrm{K} - \mathrm{M} - \overline{\mathrm{K}} - \Gamma$ path will be discussed later (Fig. 3.10).
Furthermore, it is interesting for the later discussion to choose a larger distance of the silver atoms to the top layer of silicon atoms of 4.337 Å (Fig. 3.3 e)). The band structure is displayed in Fig. 3.11. There is no hybridization of silver and silicon anymore and the material is a metal.

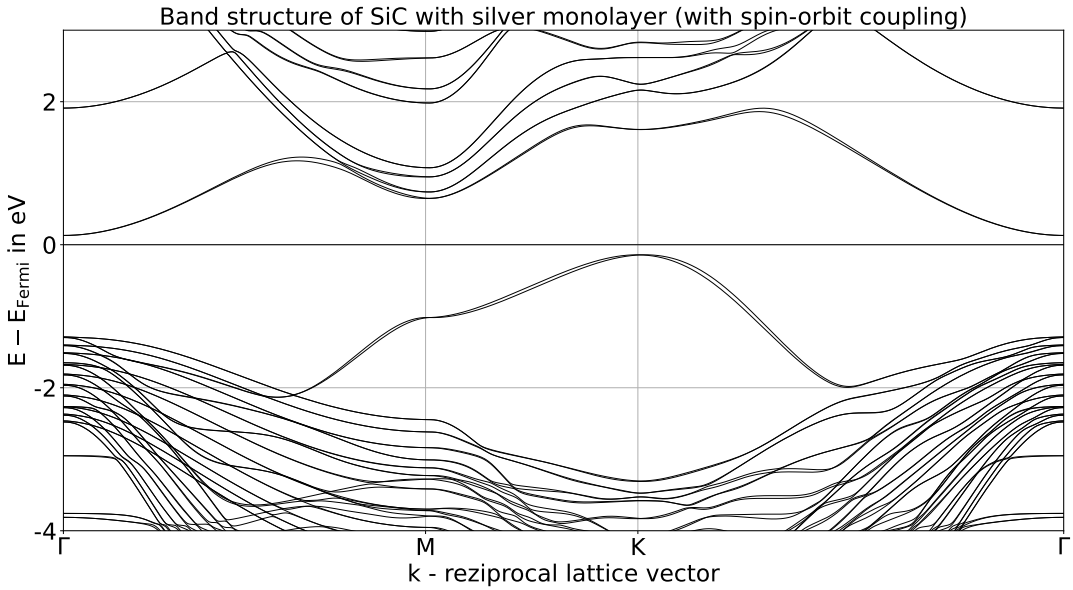

Figure 3.8: Band structure of silicon carbide with silver monolayer and H termination in the $\Gamma - \mathrm{M} - \mathrm{K} - \Gamma$ path.

Errors in DFT band gaps obtained from calculations can be attributed to two sources: Firstly, the exchange correlation functional is an approximation. Secondly, there is a derivative discontinuity term, originating from the true density functional, which is discontinuous with the total number of electrons in the system [14].

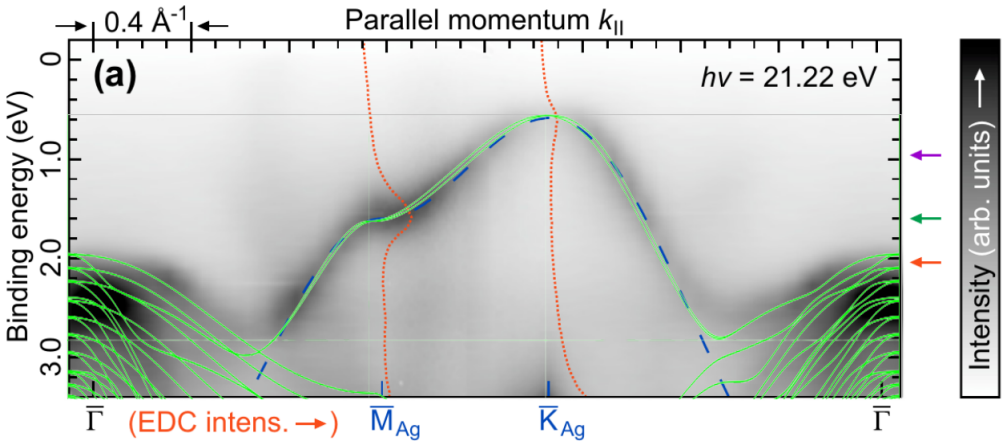

Figure 3.9: Experimental data of the band structure of a silver monolayer intercalated between silicon carbide and epitaxial buffer layer graphene [20]. They used angle-resolved photoelectron spectroscopy. The dashed blue curve represents a next-nearest-neighbor tight-binding model fitted to the Ag-induced valence band away from $\overline{\Gamma}$. Energy distribution curves at $\overline{K}_{Ag}$ and $\overline{M}_{Ag}$ are overlayed (dashed orange). The theoretical calculated band structure of a silver monolayer on top of SiC from Fig. 3.8 is superimposed in green.

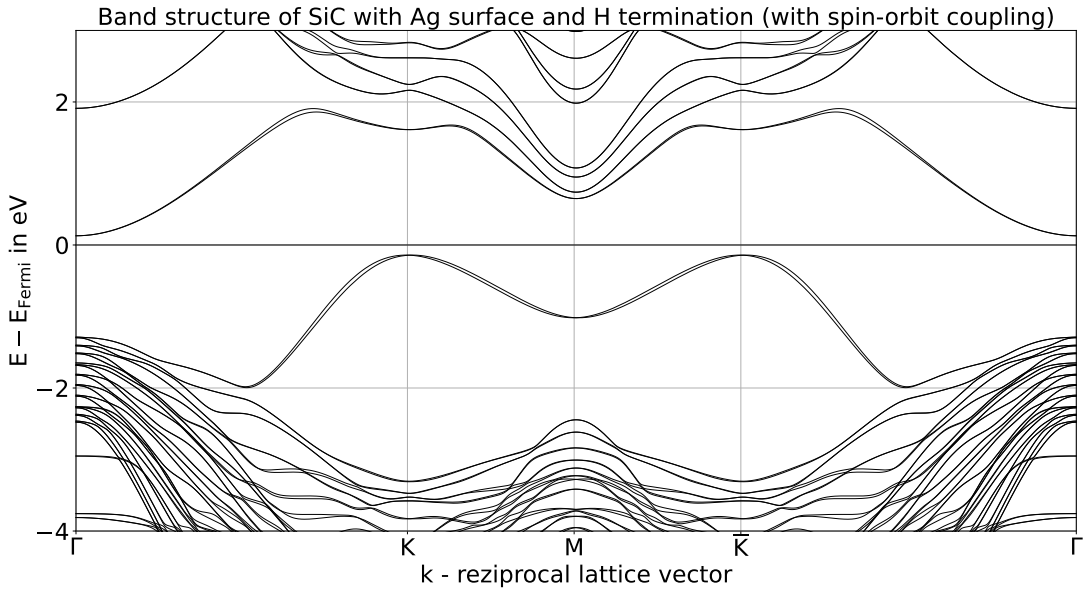

Figure 3.10: Band structure of silicon carbide with silver monolayer and H termination in the $\Gamma - K - M - \overline{K} - \Gamma$ path.

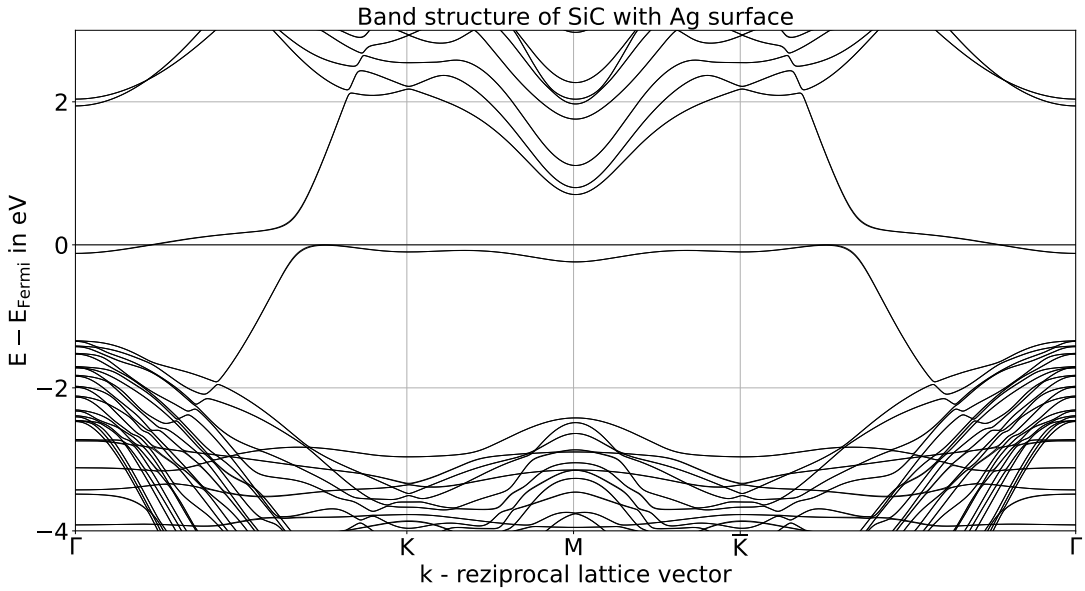

Figure 3.11: Band structure of silicon carbide with silver monolayer and H termination $\Gamma - \mathrm{K} - \mathrm{M} - \overline{\mathrm{K}} - \Gamma$ path with a distance of 4.337Å between silver and silicon atoms in the z coordinate.

4 Optical properties and symmetry breaking of two-dimensional silver on silicon carbide

First, this chapter will introduce the concept of valley-selective circular dichroism. Afterwards, the results in form of the valley-resolved dielectric function, valley polarization and the orbital angular momentum are reported for the SiC slab with and without silver. At the end, we analyze a band splitting for the Rashba effect and discuss symmetry breaking.

4.1 Theoretical background

Circular dichroism is the differential absorption of a material to left and right-handed circularly polarized light. This work explores the emergence of *Valley-selective circular dichroism* (VCD) due to substrate-induced breaking of inversion symmetry. Here, valley denote the two-fold degenerate pockets, which emerge in the valence and conduction bands. For VCD, the total absorption of the material shows no difference between left- and right-handed polarized light. Conversely, the absorption at the K and $\overline{\mathrm{K}}$ high symmetry points in the first Brillouin zone can depend on light chirality in hexagonal lattice. VCD can experimentally be detected using for example photoemission spectroscopy, see [3].
Valleytronics is the technology of control over the valley degree of freedom in multivalley semiconductors. For making valleytronic devices it is necessary to strive for valley polarization, which means to only have optical transitions at one valley. The next challenge is to detect the resulting valley-polarized current [2].
If a material has no inversion center, there is an inversion asymmetry of the potential within a unit cell. In combination with strong spin-orbit coupling and a large band gap, this allows valley polarization to be achieved. Incoming photons with a given circular polarization will mainly excite electrons within a particular valley. In this context, the absence of inversion symmetry is the source of the chiral response to light [2].
Caruso et al.[7] developed a many-body formalism based on the Bethe-Salpeter equation (BSE) to investigate the chirality of valley excitons formed in two-dimensional honeycomb lattices upon absorption of circularly polarized light. With that, the orbital angular momentum (OAM) of valley excitons can be directly estimated from the exciton wave function.

The absorption of circularly polarized light is governed by the formation of bound electron-hole pairs (excitons) at the K or $\overline{\mathrm{K}}$ valleys in the BZ depending on the light helicity. The establishing of an imbalance in the populations of the K and $\overline{\mathrm{K}}$ valleys enables the exploitations of valley degrees of freedom. Thus, VCD has become a central element for valleytronic applications [7].
The dielectric function describes the electric polarizability of a dielectric in dependence of an applied electromagnetic field:

$$\epsilon(\omega, \mathbf{k}) = \epsilon_1(\omega, \mathbf{k}) + i\epsilon_2(\omega, \mathbf{k}). \tag{4.1}$$

ϵ_1 is related to the polarizability and ϵ_2 to the absorption. To investigate the influence of light polarization on the bound excitons formed at the K and $\overline{\mathrm{K}}$ valleys, the imaginary part ϵ_2 is considered:

$$\epsilon_2 = \frac{4\pi^2 e^2}{m_e^2 \Omega N_k} \sum_{\lambda} |\hat{\epsilon} \cdot \mathbf{t}^{\lambda}|^2 \delta(E^{\lambda} - \hbar\omega) \tag{4.2}$$

where $\hat{\epsilon}$ denotes the light-polarization unitary vector, Ω the unit cell volume, N_k the number of k points and $\mathbf{t}^{\lambda}$ the transition coefficients [7].
Regarding the total absorption, the dielectric function is independent of the in-plane orientation of the light-polarization vector $\hat{\epsilon}$.

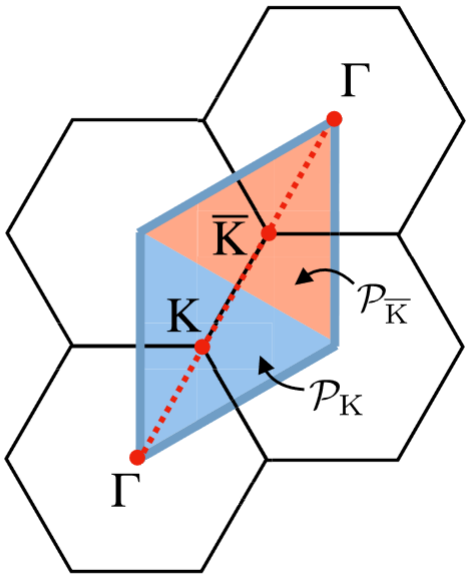

Figure 4.1: The Brillouin zone of a hexagonal system is framed by blue lines. The blue and orange shadings mark the $\mathcal{P}_K$ and $\mathcal{P}_{\overline{K}}$ regions in the BZ, respectively. The $\Gamma - \mathrm{K} - \mathrm{M} - \overline{\mathrm{K}} - \Gamma$ path is shown as a dotted red line [7].

Following Caruso et al. [7], the first BZ can be divided into the regions $\mathcal{P}_K$ and $\mathcal{P}_{\overline{K}}$ which enclose K and $\overline{\text{K}}$ respectively (Fig. 4.1). The valley resolved transition coefficient $\mathbf{t}_K^\lambda$ ($\mathbf{t}_{\overline{K}}^\lambda$) includes only the electron-hole transition in $\mathcal{P}_K$ ($\mathcal{P}_{\overline{K}}$). The additivity condition is exactly satisfied ($\mathbf{t}^\lambda = \mathbf{t}_K^\lambda + \mathbf{t}_{\overline{K}}^\lambda$). Nonetheless, the contribution of the $\mathcal{P}_K$ and $\mathcal{P}_{\overline{K}}$ regions to the dielectric function can be separated only by approximation and only close to the absorption onset. The valley-resolved dielectric function $\epsilon_{2,K}$ ($\epsilon_{2,\overline{K}}$) accounts only for absorption processes resulting from the excitation of electron-hole pairs within the K ($\overline{\text{K}}$) valley. In the vicinity of the absorption onset, $\epsilon_2(\omega) \approx \epsilon_{2,K}(\omega) + \epsilon_{2,\overline{K}}(\omega)$ is a good approximation. For left-handed (+) and right-handed (-) circularly polarized light, the light polarization vector $\hat{\epsilon}$ can be expressed as

$$\hat{\epsilon}_\pm = \frac{\hat{\mathbf{x}} \pm i\hat{\mathbf{y}}}{\sqrt{2}}, \tag{4.3}$$

where $\hat{\mathbf{x}}$ and $\hat{\mathbf{y}}$ are Cartesian unit vectors. The transverse dielectric function at K for circularly polarized light is

$$\epsilon_{2,K}^{(\pm)}(\omega) = \frac{1}{2}\left[\xi_{xx}^K(\omega) + \xi_{yy}^K(\omega)\right] \mp Im\left[\xi_{xy}^K(\omega)\right] \tag{4.4}$$

with the dichroic tensor

$$\xi_{\alpha,\beta}^K(\omega) = \frac{4\pi^2 e^2}{m_e^2 \Omega N_k} \sum_\lambda (\mathbf{t}_K^{\lambda,\alpha})^* \mathbf{t}_K^{\lambda,\beta} \delta(E^\lambda - \hbar\omega). \tag{4.5}$$

The same applies to $\overline{\text{K}}$ instead of K. The relation between the dichroic and the dielectric tensor is discussed in the Supporting Information[1] by [7].
The emergence of valley-selective circular dichroism can be quantified by the differential dichroic absorption

$$D_K(\omega) = \epsilon_{2,K}^{(+)}(\omega) - \epsilon_{2,K}^{(-)}(\omega) = -2Im\left[\xi_{xy}^K(\omega)\right]. \tag{4.6}$$

The valley-resolved components of the dichroic tensor are finite and opposite in sign at K and $\overline{\text{K}}$ ($Im[\xi_{xy}^K] = -Im[\xi_{xy}^{\overline{\text{K}}}] \neq 0$). This indicates that the individual valleys are characterized by a non-trivial chiral character, leading to non-disappearing differential dichroic absorption in $\mathcal{P}_K$ and $\mathcal{P}_{\overline{K}}$ [7].
For linear polarization, it can be $\hat{\epsilon} = \hat{\mathbf{x}}$. Thus, the absorption in the K and $\overline{\text{K}}$ valleys is described by the xx components of the corresponding valley-resolved dielectric tensors. There is an identical response of $\epsilon_{2,K}^{xx}$ and $\epsilon_{2,\overline{K}}^{xx}$ for all photon energies and thus the probability for light absorption at K or $\overline{\text{K}}$ is the same [7].
In contrast, the valley-resolved dielectric functions for left and right-handed polarized light are different. For left-handed polarization, the light is almost exclusively absorbed in the $\mathcal{P}_K$ region of the BZ in the vicinity of the absorption onset [7].

[1] https://pubs.acs.org/doi/suppl/10.1021/acs.jpclett.2c01034/suppl_file/jz2c01034_si_001.pdf

In Quantum mechanics, the angular-momentum operator has the same relation as the angular-momentum in classical physics but with operators:

$$\hat{\mathbf{L}} = \hat{\mathbf{r}} \times \hat{\mathbf{p}}. \tag{4.7}$$

With the momentum operator $\hat{\mathbf{p}} = -i\hbar\nabla$, the z-component becomes [24]

$$\hat{\mathrm{L}}_\mathrm{z} = -i\hbar\frac{\partial}{\partial\phi}. \tag{4.8}$$

Applying the operator on a eigenfunction of the orbital angular momentum Y_{lm} delivers the orbital angular momentum m:

$$\hat{\mathrm{L}}_\mathrm{z} Y_{lm} = \hbar m Y_{lm} \tag{4.9}$$

with $m = -l, ..., l$ where $l = 0, 1, 2, ...$ is the orbital quantum number.
Nonetheless, this does not apply for a solid. A solid consists of unit cells and periodic boundary conditions, which has an influence to the orbital angular momentum (OAM). Here, we will not derive the correct expression but write the OAM for a solid as $l^z_{\mathbf{nk}}$. It is implemented in the code provided by Caruso et al.[7].

4.2 Calculations for the optical properties

The valley-resolved dielectric function from equation (4.4) is calculated at the K valley with linear and left-handed polarized light for the constructed system of the SiC surface with the silver monolayer (Fig. 4.2). For linear polarized light, the absorption at K and $\overline{\mathrm{K}}$ coincides for all energies. For circular polarization, there is a difference in the absorption at K and $\overline{\mathrm{K}}$. The total absorption shows a peak around 2 eV, which is probably due to the band gap. These results indicate the emergence of VCD.
Only optical transitions up to 6 eV are considered. For higher energies artifacts may occur within the slab model. Therefore, the valley-resolved dielectric function for a vacuum space of 25 Å and 35 Å have been evaluated, see Fig. 6.4 in the appendix.
The valley polarization for left-handed circularly polarized light is defined as

$$\eta^{(+)} = \frac{|\epsilon^{(+)}_{2,\mathrm{K}} - \epsilon^{(+)}_{2,\overline{\mathrm{K}}}|}{|\epsilon^{(+)}_{2,\mathrm{K}} + \epsilon^{(+)}_{2,\overline{\mathrm{K}}}|}. \tag{4.10}$$

η ranges between zero and one, where one indicates complete valley polarization. Fig. 4.3 shows the valley polarization η as a function of energy. It shows a maximum valley polarization of about 60% for energies up to 6 eV. Most optical transitions happen in the energy range of 1.4 and 2.4 eV which is marked in blue. The mean valley polarization for this range is 39%. Values under 1.4 eV are not displayed in this diagram because the energies are smaller than direct optical transitions from the valence band to the conduction band.

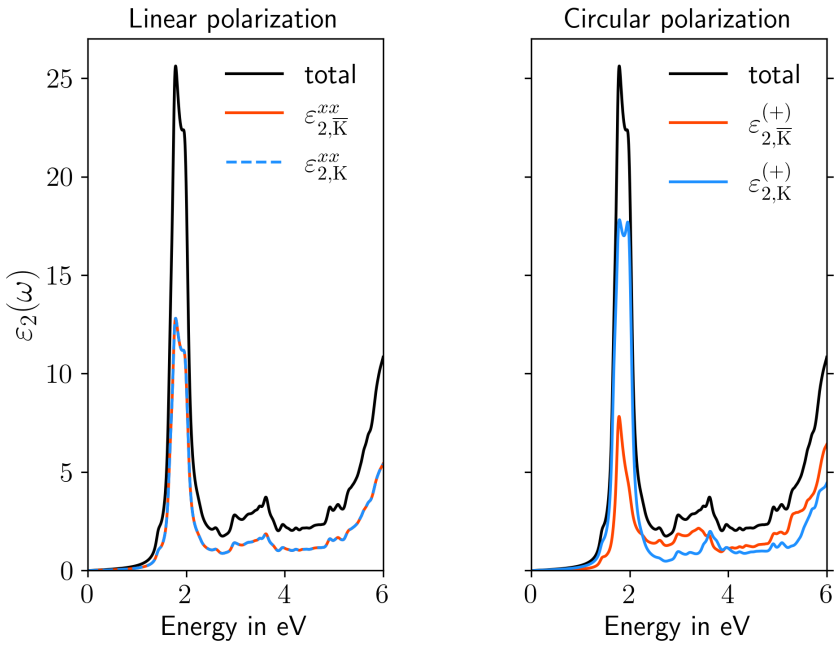

Figure 4.2: The imaginary part of the dielectric function for linearly and left-handed circularly polarized light shining on SiC with a silver monolayer in the K valley in blue, in the $\overline{\mathrm{K}}$ valley in orange and in total in black.

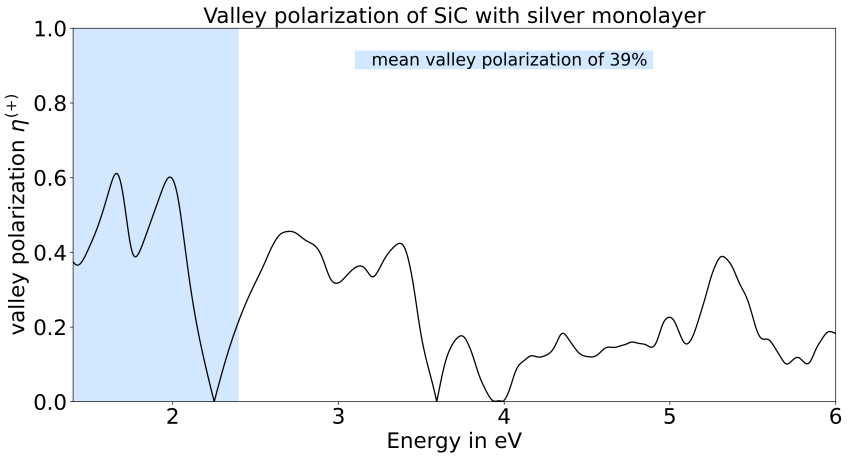

Figure 4.3: Valley polarization for silicon carbide with silver monolayer.

In Fig. 4.4, the OAM is evaluated. Therefore, the colour represents the orientation and the intensity of the value of $\mathrm{l}_{\mathrm{n},\mathbf{k}}{}^{z}$. The scale on the right represents a value for a defined intensity of the colour. In the band structure, the OAM is symmetric to the M axis with a different sign. The top valence band and the bottom conduction band have defined orientations of the OAM at the K and $\overline{\mathrm{K}}$ valley.
The OAM for the top valence band is shown in Fig. 4.5. It shows, that there are

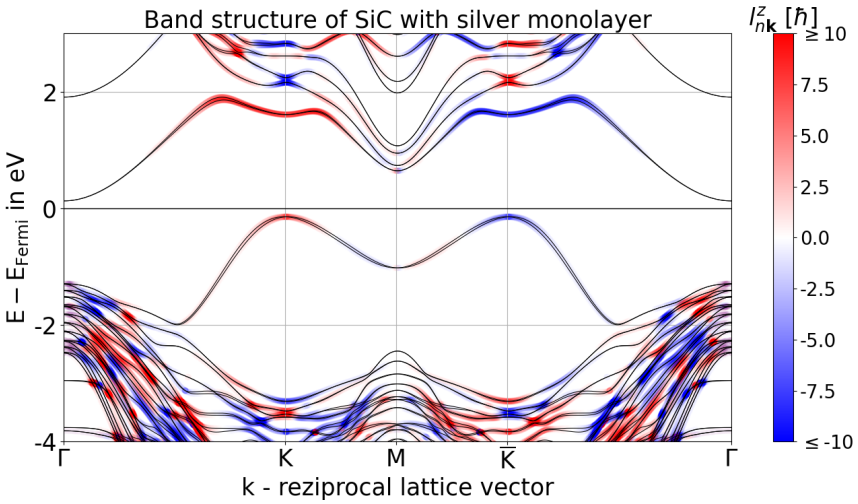

Figure 4.4: Orbital angular momentum superimposed on the band structure of SiC with silver monolayer for momenta along the $\Gamma - \mathrm{K} - \mathrm{M} - \overline{\mathrm{K}} - \Gamma$ line.

peaks at K and $\overline{\mathrm{K}}$ with a different orientation of the OAM.

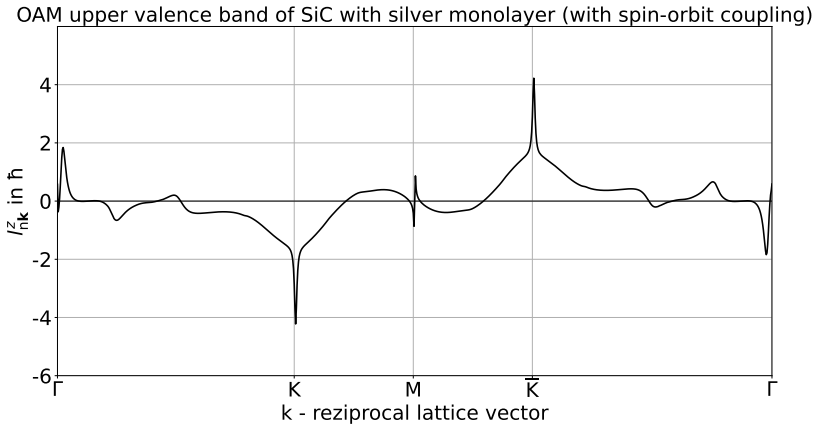

Figure 4.5: Orbital angular momentum for the top valence band of SiC with silver monolayer for momenta along the $\Gamma - \mathrm{K} - \mathrm{M} - \overline{\mathrm{K}} - \Gamma$ line.

These results show, that there is VCD for the calculated structure of SiC with silver monolayer.
Since SiC itself has also no inversion center, it should also show valley-selective circular dichroism. The valley-resolved dielectric function for the SiC surface with H termination is shown in Fig. 4.6.
The valley polarization (Fig. 4.7) has a maximum of 49% for energies up to 6 eV. The energy gap for direct optical transitions begins at 2.3 eV. Taking a range of 1 eV, the mean valley polarization is 13%. The effect of VCD without silver is smaller.

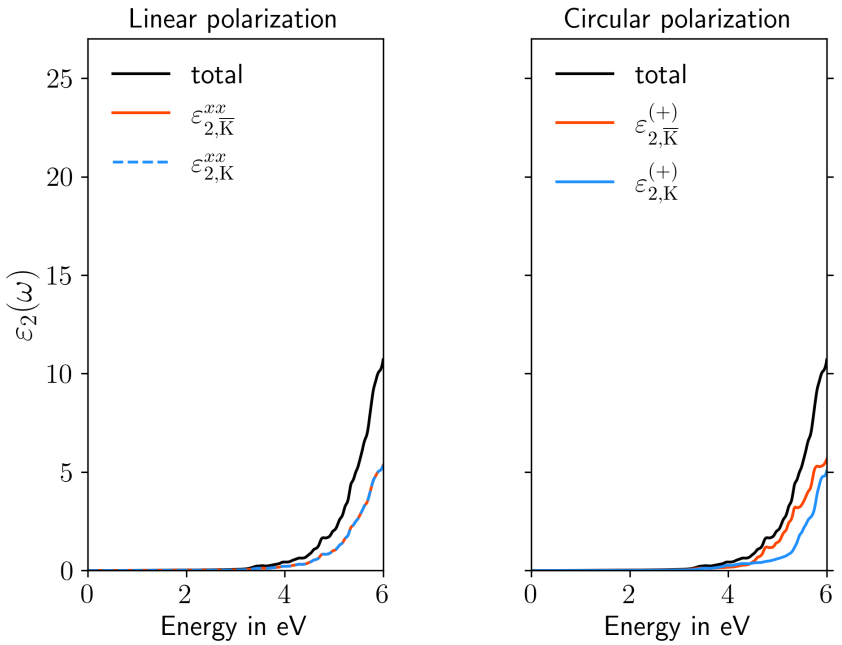

Figure 4.6: The imaginary part of the dielectric function for linearly and left-handed circularly polarized light shining on SiC in the K valley in blue, in the $\overline{\mathrm{K}}$ valley in orange and in total in black.

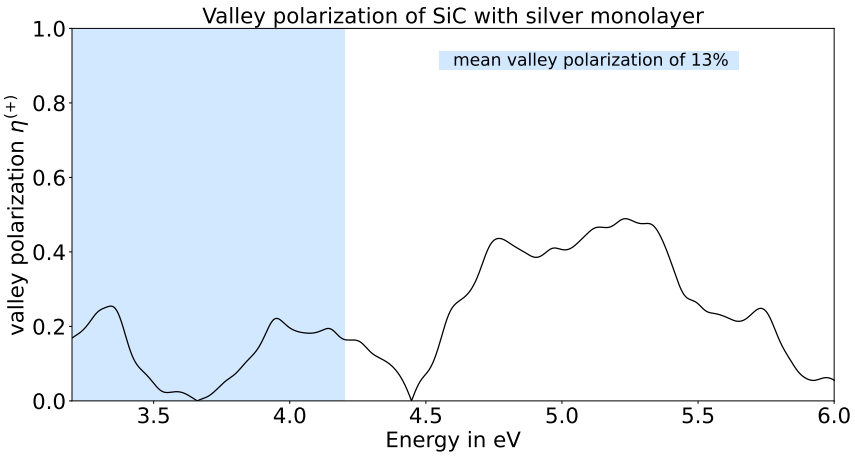

Figure 4.7: Valley polarization for silicon carbide surface with H termination.

Furthermore, the total absorption for smaller energies is lower because the band gap is larger.

The optical properties of two-dimensional silver itself can not be investigated here because the code provided by Caruso et al.[7] is not implemented for metals but only for semiconductors.

4.3 Rashba effect and symmetry breaking

By taking a closer look to the band structure of SiC with silver monolayer in the $\Gamma - \mathrm{K} - \mathrm{M} - \overline{\mathrm{K}} - \Gamma$ path (Fig. 3.10), one can see a splitting of the highest bands in the valence band around the K and $\overline{\mathrm{K}}$ valley to the sides. One of the bands is characterized by spin up and the other one by spin down.
"Spin-orbit coupling is the dipole interaction between the spin of an electron and the magnetic field created by the electron's own orbital motion"[24]. In the nucleus rest frame, the electron is orbiting an atom. In an inertial frame comoving with the electron, the nucleus appears to be orbiting the atom. The orbiting nucleus constitutes a current which gives rise to a magnetic field at the origin equal to

$$\mathbf{B} = \frac{\mathbf{E} \times \mathbf{v}}{c^2} \tag{4.11}$$

where

$$\mathbf{E} = -\nabla V(r) \tag{4.12}$$

is the electric field at the electron due to the nucleus and V(r) is the corresponding potential energy. Equation (4.11) ia a result from the transformation of electric and magnetic fields in special relativity [5]. The Hamiltonian which is responsible for the spin-orbit coupling of a free electron propagation in an electric field can be directly derived from the Dirac equation by a power expansion in $(v/c)^2$ in the nonrelativistic approximation:

$$\hat{H}_{SO} = -\frac{1}{4c^2}\vec{\sigma}(\hat{\mathbf{p}} \times \vec{\nabla} V), \tag{4.13}$$

with $\mathbf{p}$ the momentum and $\vec{\sigma}$ the Pauli spin matrices. This operator contributes to the total Hamiltonian and is called Pauli spin-orbit term. Assuming a radially symmetric potential V results in the well-known spin-orbit coupling Hamiltonian in atomic physics:

$$\hat{H}_{SO} = \frac{1}{2c^2 r}\frac{dV(r)}{dr}\mathbf{S} \cdot \mathbf{L}. \tag{4.14}$$

Here, the spin is $\mathbf{S} = \frac{1}{2}\vec{\sigma}$ and the orbital angular momentum $\mathbf{L} = \mathbf{r} \times \mathbf{p}$ [21].
Each eigenstate $\epsilon_{\uparrow\downarrow}(k)$ is two-fold degenerate for spin-up and spin-down electrons. This is a consequence of inversion symmetry of both space and time. Space inversion symmetry changes the wave vector k into -k and for each spin-direction σ, $\sigma \in \{\uparrow, \downarrow\}$, the single-particle energy transforms as $\epsilon_\sigma(k) = \epsilon_\sigma(-k)$. In addition, time inversion symmetry flips the spin, $\epsilon_\uparrow(k) = \epsilon_\downarrow(-k)$, known as the *Kramers degeneracy* of the single-particle states. If we combine both symmetry operations, we get that the two-fold degeneracy of the single-particle energies is $\epsilon_\uparrow(k) = \epsilon_\downarrow(k)$. The spin-degeneracy is removed when the potential through which the electrons move is inversion-asymmetric even if there is no external magnetic field B. The inversion asymmetry of the potential $V(r)$ is characterized by an electric field $\mathbf{E}$. When electrons are subject to an external electric field E defined in a global frame of reference, then the relativistic Lorentz transformation gives rise to the magnetic field B (eq.

4.11) in the local frame of the moving electron. The interaction of the spin with this B field leads then to the *Rashba* or *Bychkov-Rashba* Hamiltonian

$$\hat{H}_R = \alpha_{\mathrm{R}} \vec{\sigma}(\mathbf{p} \times \mathbf{E}). \tag{4.15}$$

It describes an additional contribution to the kinetic energy which leads then to the structure inversion-asymmetric spin splitting, the Rashba effect [12]. The parameter α_{R} is the *Rashba parameter* which gives a value for the strength of the spin-orbit coupling [21].

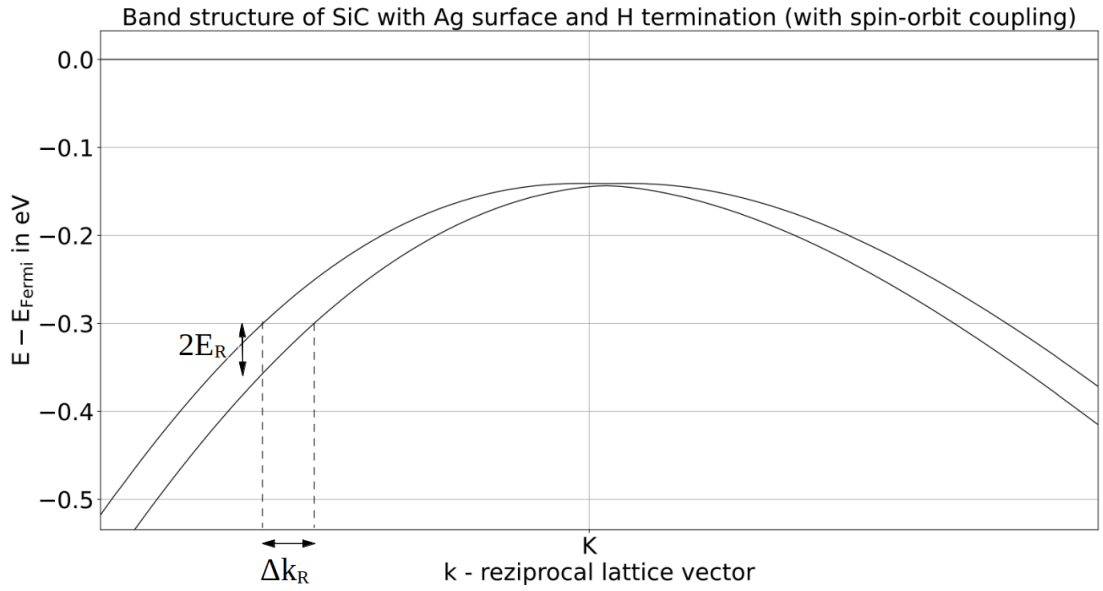

Figure 4.8: Evaluation of the band splitting around the K valley of the highest valence band of SiC with silver monolayer.

Fig. 4.8 shows a zoom from Fig. 3.10 to the region of band splitting around the K high symmetry point. The shift in the reciprocal space is $\Delta k_R \approx 0.026$ Å^{-1}. This is in good agreement to other studies of the Rashba effect, for example Bihlmayer et al. [4] found a shift of $\Delta k_R \approx 0.022$ Å^{-1} for a Ag(111) surface. The difference in energy for $|\mathbf{k}| = 1.19$ Å^{-1} is $2E_{\mathrm{R}} = 70$ meV. The relation of E_{R} and $|\mathbf{k}|$ is proportional to the Rashba parameter α_{R} [21]

$$E_{\mathrm{R}} = \pm \alpha_{\mathrm{R}} |\mathbf{k}| \tag{4.16}$$

and thus the Rashba parameter is $\alpha_{\mathrm{R}} \approx 5.88 \times 10^{-12}$ m $\cdot$ eV.
In contrast, there is no band splitting to the sides in Fig. 3.11 where the distance of the silver atoms is increased so that there is no hybridization with the silicon atoms anymore. The Rashba effect only takes place when there is a hybridization of silver and silicon.
One can also think of the Dresselhaus effect, which appears in the same way in a band structure, but the Dresselhaus effect is related to the absence of a bulk

inversion center [21]. A band splitting is not visible in the band structure of SiC (Fig.3.4) though SiC lacks inversion symmetry.
Moreover, the Rashba effect is particularly strong for crystals containing atoms with a large atomic number because the electrons also experience the potential gradient due to the electron orbitals of the atoms forming the crystal [21]. That means, that it is likely that the Rashba effect is related to the silver atoms which have a much larger atomic number of 47 than silicon and carbon, which have 14 and 6, respectively. Indeed, the bands, which are split in Fig.3.10, are related to the hybridization of the silver atoms because the band with the saddel point at M and the maximum at K in Fig. 3.8 shows the same structure as in the band structure of two-dimensional silver (Fig. 3.2). That means, SiC breaks the inversion symmetry of two-dimensional silver which induces the Rashba effect.
Spatial inversion symmetry contain inversion centers. If the inversion center is in the origin, for every point (x, y, z) in the lattice there is an indistinguishable point (-x, -y, -z). On the one hand, a surface is created which automatically has no inversion symmetry because there are silicon and carbon atoms under the silver monolayer but not above. On the other hand, looking at Fig. 3.7, the silver atoms no longer contain inversion centers because the carbon atoms can not be reflected to the other side on a silver atom. Furthermore, the underlying SiC influences the electron density of the two-dimensional silver plane. The chemical bonding of the silicon and silver atoms changes the density of the electronic structure directly. This breaks the symmetry of the Kohn-Sham orbitals.

5 Conclusion and Outlook

In this thesis, I investigated the influence of substrate-induced symmetry breaking on two-dimensional silver. The main findings of this thesis are that silicon carbide breaks the inversion symmetry of two-dimensional silver and induces valley-selective circular dichroism.
Silicon carbide with a monolayer silver from Fig. 1.1 is constructed using a 6H-SiC polytype. The silver atoms are also arranged in a hexagonal lattice with the same lattice constant as SiC. A hybridization between the silver and silicon atoms takes place. The quasi-free standing epitaxial graphene bilayer is neglected. The band structure is calculated using DFT code from QUANTUM ESPRESSO and it shows very good agreement to experimental data.
The substrate SiC breaks the inversion symmetry of two-dimensional silver. This influence is directly observable in the band structure as a band splitting because of the Rashba effect. SiC has no inversion center and shows properties of valley-selective dichroism. Nonetheless, valley-selective dichroism becomes even more revealed when a silver monolayer is on top of a SiC surface. This material is a semiconductor with a small band gap. In combination with valley-selective circular dichroism, it is very interesting for the field of valleytronics.
One research area of valleytronics is quantum manipulation of valleys in semiconductors including quantum computation with valley-based qubits. For example, Culcer et al.[8] worked on "Valley-Based Noise-Resistant Quantum Computation Using Si Quantum Dots" and Laird et al.[17] on "A valley–spin qubit in a carbon nanotube". Since quantum computation is one of the great scientific hopes and challenges of this century, there is a lot of potential in this field of research.

6 Appendix

6.1 Convergency tests for SiC with silver monolayer

The total energy in Fig. 6.2, 6.3 and 6.1 does converge for the number of k points, the cutoff energy and the distance between the slabs.
The distance of the slabs is chosen to be 25 Å which has an error of $1.18 \cdot 10^{-2}\%$ in total energy compared to a distance of 45 Å.

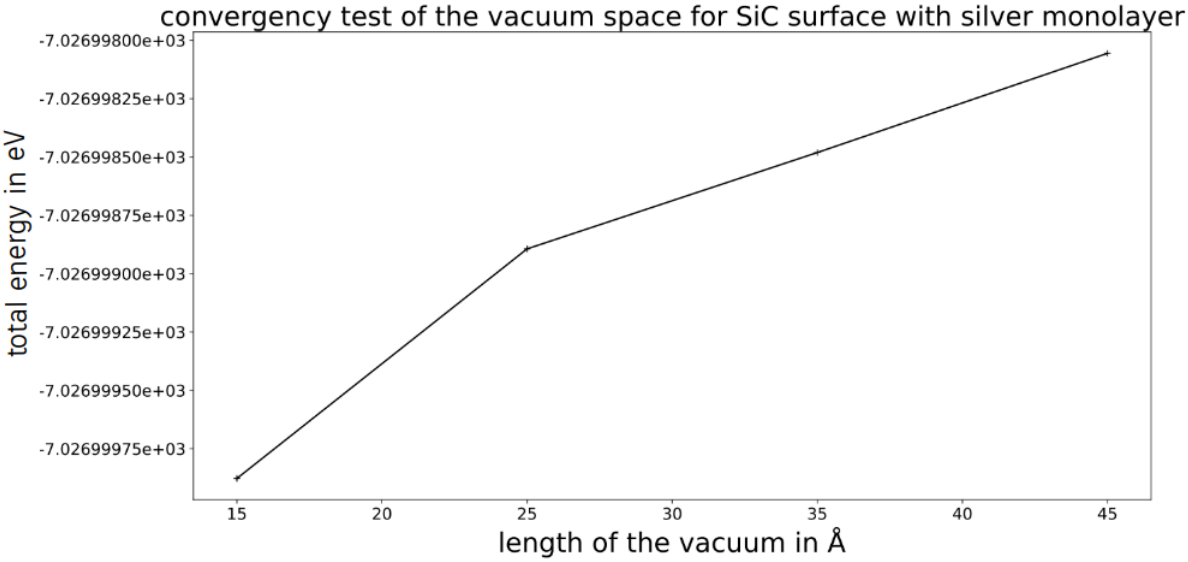

Figure 6.1: Total energy as a function of the vacuum space between slabs, obtained from DFT-PBE calculations.

12 k points in the x and y direction are chosen for this work which is an error of $6.85 \cdot 10^{-7}\%$ in total energy compared to 18 k points. QUANTUM ESPRESSO reduces the number of k points used to take advantage of the symmetry to in total 19 and 37 k points, respectively.
For the cutoff energy, 70 eV is chosen which is an error of $1.82 \cdot 10^{-3}\%$ in total energy compared to 90 eV.

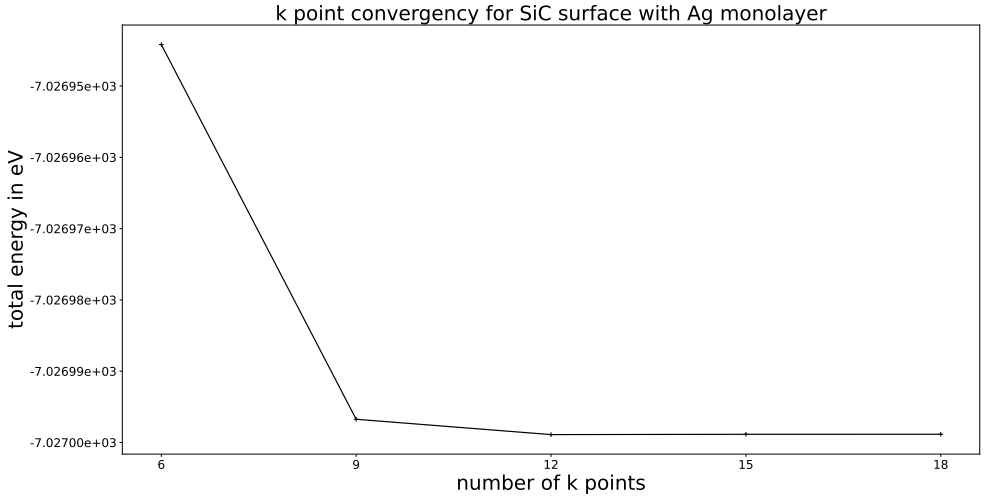

Figure 6.2: Total energy as a function of the number of k points, obtained from DFT-PBE calculations.

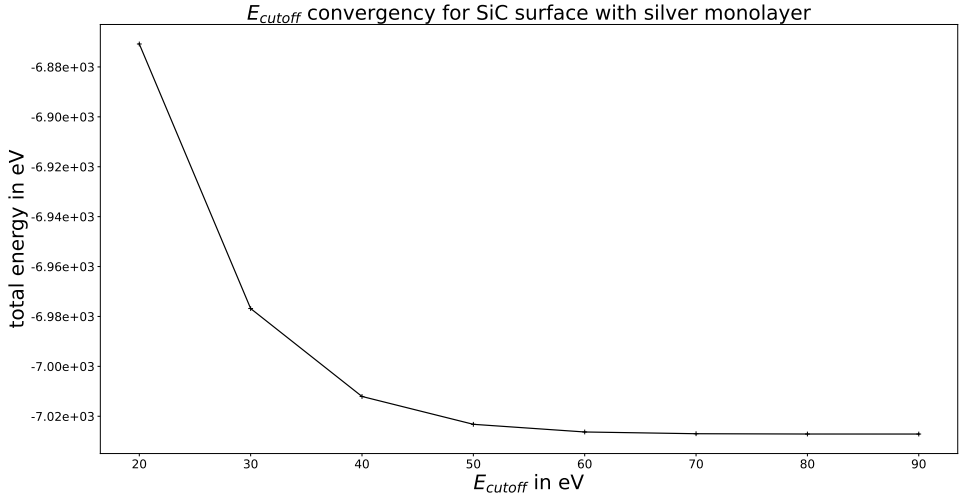

Figure 6.3: Total energy as a function of the kinetic energy cutoff E_{cutoff}, obtained from DFT-PBE calculations.

6.2 Valley polarization

The absolute difference in valley polarization of a slab model with a vacuum of 25 Å and 35 Å is shown in Fig. 6.4. Since there is an increase in the difference from 6 eV on, only values up to 6 eV are considered for the evaluation of the valley-resolved dielectric function.

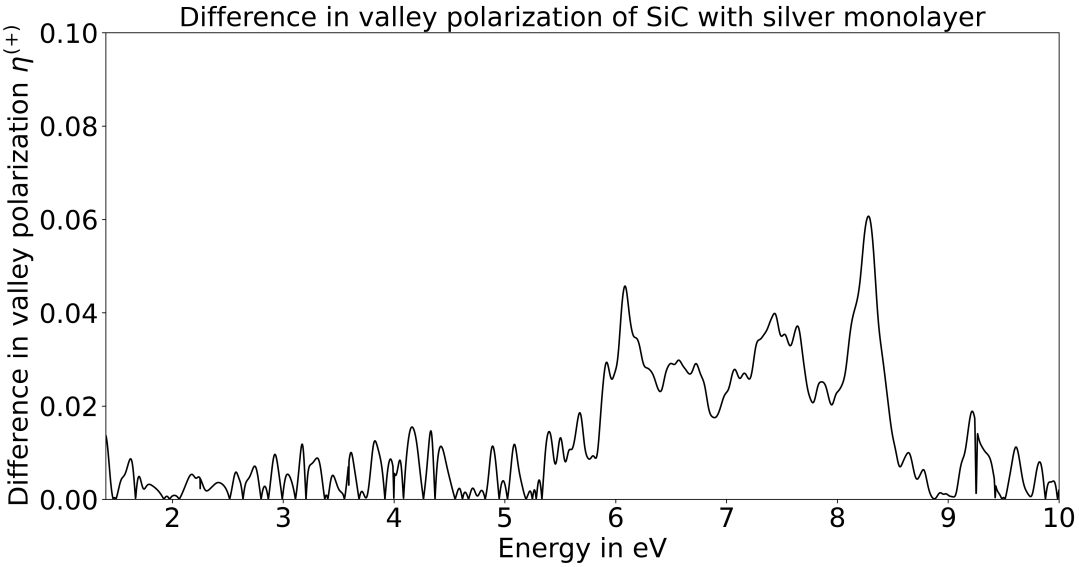

Figure 6.4: The difference in valley polarization for SiC with silver monolayer for a vacuum of 25 Å and 35 Å

Bibliography

[1] M. I. Aroyo, editor. *International Tables for Crystallography*. International Union of Crystallography, December 2016.

[2] Kamran Behnia. Polarized light boosts valleytronics. *Nature Nanotechnology*, 7(8):488–489, July 2012.

[3] H. Beyer, G. Rohde, A. Grubišić Čabo, A. Stange, T. Jacobsen, L. Bignardi, D. Lizzit, P. Lacovig, C. E. Sanders, S. Lizzit, K. Rossnagel, P. Hofmann, and M. Bauer. 80% valley polarization of free carriers in singly oriented single-layer ws2 on au(111). *Physical Review Letters*, 123(23), December 2019.

[4] G. Bihlmayer, Yu.M. Koroteev, P.M. Echenique, E.V. Chulkov, and S. Blügel. The rashba-effect at metallic surfaces. *Surface Science*, 600(18):3888–3891, September 2006.

[5] Stephen Blundell. *Magnetism in Condensed Matter*. Oxford University Press, January 2001.

[6] Natalie Briggs, Zewdu M. Gebeyehu, Alexander Vera, Tian Zhao, Ke Wang, Ana De La Fuente Duran, Brian Bersch, Timothy Bowen, Kenneth L. Knappenberger, and Joshua A. Robinson. Epitaxial graphene/silicon carbide intercalation: a minireview on graphene modulation and unique 2d materials. *Nanoscale*, 11(33):15440–15447, 2019.

[7] Fabio Caruso, Maximilian Schebek, Yiming Pan, Cecilia Vona, and Claudia Draxl. Chirality of valley excitons in monolayer transition-metal dichalcogenides. *The Journal of Physical Chemistry Letters*, 13(25):5894–5899, June 2022.

[8] Dimitrie Culcer, A. L. Saraiva, Belita Koiller, Xuedong Hu, and S. Das Sarma. Valley-based noise-resistant quantum computation using si quantum dots. *Physical Review Letters*, 108(12), March 2012.

[9] P. Giannozzi, S. Baroni, N. Bonini, M. Calandra, R. Car, C. Cavazzoni, D. Ceresoli, G. L. Chiarotti, m. Cococcioni, I. Dabo, A. Dal Corso, S. Fabris, G. Fratesi, S. de Gironcoli, R. Gebauer, U. Gerstmann, C. Gougoussis, A. Kokalj, M. Lazzeri, L. Martin-Samos, N. Marzari, F. Mauri, R. Mazzarello, S. Paolini, A. Pasquarello, L. Paulatto, C. Sbraccia, S. Scandolo, G. Sclauzero, A. P. Seitsonen, A. Smogunov, P. Umari, and R. M. Wentzcovitch. Quantum

espresso: a modular and open-source software project for quantum simulations of materials. 2009.

[10] Feliciano Giustino. *Materials Modelling Using Density Functional Theory: Properties and Predictions*. Oxford University Press, Oxford, 2014.

[11] Axel Groß. *Theoretical Surface Science*. Springer Berlin Heidelberg, 2009.

[12] M. Heide, G. Bihlmayer, Ph. Mavropoulos, A. Bringer, and S. Blügel. *Spin Orbit Driven Physics at Surfaces*. International Union of Crystallography, 2006.

[13] P. Hohenberg and W. Kohn. Inhomogeneous electron gas. *Physical Review*, 136(3B):B864–B871, November 1964.

[14] Anubhav Jain, Geoffroy Hautier, Charles J. Moore, Shyue Ping Ong, Christopher C. Fischer, Tim Mueller, Kristin A. Persson, and Gerbrand Ceder. A high-throughput infrastructure for density functional theory calculations. *Computational Materials Science*, 50(8):2295–2310, June 2011.

[15] Anubhav Jain, Shyue Ping Ong, Geoffroy Hautier, Wei Chen, William Davidson Richards, Stephen Dacek, Shreyas Cholia, Dan Gunter, David Skinner, Gerbrand Ceder, and Kristin A. Persson. Commentary: The materials project: A materials genome approach to accelerating materials innovation. *APL Materials*, 1(1):011002, July 2013.

[16] G. Kresse and D. Joubert. From ultrasoft pseudopotentials to the projector augmented-wave method. *Physical Review B*, 59(3):1758–1775, January 1999.

[17] E. A. Laird, F. Pei, and L. P. Kouwenhoven. A valley–spin qubit in a carbon nanotube. *Nature Nanotechnology*, 8(8):565–568, July 2013.

[18] Woojoo Lee, Yuanxi Wang, Wei Qin, Hyunsue Kim, Mengke Liu, T. Nathan Nunley, Bin Fang, Rinu Maniyara, Chengye Dong, Joshua A. Robinson, Vincent Crespi, Xiaoqin Li, Allan H. MacDonald, and Chih-Kang Shih. Confined monolayer ag as a large gap 2d semiconductor and its momentum resolved excited states. 2022.

[19] Hendrik J. Monkhorst and James D. Pack. Special points for brillouin-zone integrations. *Physical Review B*, 13(12):5188–5192, June 1976.

[20] Philipp Rosenzweig and Ulrich Starke. Large-area synthesis of a semiconducting silver monolayer via intercalation of epitaxial graphene. *Physical Review B*, 101(20), May 2020.

[21] Thomas Schäpers. *Semiconductor Spintronics*. De Gruyter, May 2021.

[22] David S. Sholl and Janice A. Steckel. *Density Functional Theory: A practical introduction*. Wiley New Jersey Canada, 2009.

[23] A. V. Sinelnik and A. V. Semenov. Theoretical study of the band structure of 2h-SiC and 4h-SiC of silicon carbide polytypes. *Condensed Matter Physics*, 24(2):23706, 2021.

[24] Ralph Skomski. *Simple Models of Magnetism*. Oxford University Press, January 2008.

[25] M.J. van Setten, M. Giantomassi, E. Bousquet, M.J. Verstraete, D.R. Hamann, X. Gonze, and G.-M. Rignanese. The PseudoDojo: Training and grading a 85 element optimized norm-conserving pseudopotential table. *Computer Physics Communications*, 226:39–54, May 2018.

[26] David Vanderbilt. Soft self-consistent pseudopotentials in a generalized eigenvalue formalism. *Physical Review B*, 41(11):7892–7895, April 1990.

Erklärung

Hiermit erkläre ich, dass ich die vorliegende Arbeit selbständig und ohne fremde Hilfe angefertigt und keine anderen als die angegebenen Quellen und Hilfsmittel verwendet habe.
Die eingereichte schriftliche Fassung der Arbeit entspricht der auf dem elektronischen Speichermedium.
Weiterhin versichere ich, dass diese Arbeit noch nicht als Abschlussarbeit an anderer Stelle vorgelegen hat.

Datum: _____ Unterschrift: _____